Journal of the American Heart Association

ORIGINAL RESEARCH

Mitral Valve Prolapse Induces Regionalized Myocardial Fibrosis

Jordan E. Morningstar, BS;* Cortney Gensemer, BS;* Reece Moore, BS; Diana Fulmer, PhD;
Tyler C. Beck, BS; Christina Wang, BS; Kelsey Moore, PhD; Lilong Guo, MD, PhD; Franz Sieg, MD;
Yasufumi Nagata, MD; Philippe Bertrand, MD; Ricardo A. Spampinato, MD; Janiece Glover, MS;
Stephen Poelzing, PhD; Robert G. Gourdie, PhD; Kelsey Watts, BS; William J. Richardson, PhD;
Robert A. Levine, MD; Michael A. Borger, MD; Russell A. Norris, PhD

BACKGROUND: Mitral valve prolapse (MVP) is one of the most common forms of cardiac valve disease and affects 2% to 3% of the population. Previous imaging reports have indicated that myocardial fibrosis is common in MVP and described its association with sudden cardiac death. These data combined with evidence for postrepair ventricular dysfunction in surgical patients with MVP support a link between fibrosis and MVP.

METHODS AND RESULTS: We performed histopathologic analysis of left ventricular (LV) biopsies from peripapillary regions, inferobasal LV wall and apex on surgical patients with MVP, as well as in a mouse model of human MVP (*Dzip1$^{S14R/+}$*). Tension-dependent molecular pathways were subsequently assessed using both computational modeling and cyclical stretch of primary human cardiac fibroblasts in vitro. Histopathology of LV biopsies revealed regionalized fibrosis in the peripapillary myocardium that correlated with increased macrophages and myofibroblasts. The MVP mouse model exhibited similar regional increases in collagen deposition that progress over time. As observed in the patient biopsies, increased macrophages and myofibroblasts were observed in fibrotic areas within the murine heart. Computational modeling revealed tension-dependent profibrotic cellular and molecular responses consistent with fibrosis locations related to valve-induced stress. These simulations also identified mechanosensing primary cilia as involved in profibrotic pathways, which was validated in vitro and in human biopsies. Finally, in vitro stretching of primary human cardiac fibroblasts showed that stretch directly activates profibrotic pathways and increases extracellular matrix protein production.

CONCLUSIONS: The presence of prominent regional LV fibrosis in patients and mice with MVP supports a relationship between MVP and progressive damaging effects on LV structure before overt alterations in cardiac function. The regionalized molecular and cellular changes suggest a reactive response of the papillary and inferobasal myocardium to increased chordal tension from a prolapsing valve. These studies raise the question whether surgical intervention on patients with MVP should occur earlier than indicated by current guidelines to prevent advanced LV fibrosis and potentially reduce residual risk of LV dysfunction and sudden cardiac death.

Key Words: computational modeling ■ DZIP1 ■ fibrosis ■ mitral valve prolapse ■ primary cilia

M itral valve prolapse (MVP) is a common degenerative disease of the left-heart inlet valve defined by billowing of one or both leaflets above the annulus. It affects 1 in 40 individuals and carries the risk of serious secondary complications such as heart failure, arrhythmias, and sudden cardiac death.[1,2] Histologically, MVP is characterized by myxomatous degeneration of the mitral leaflets, defined as loss of the normal stratified extracellular matrix layers with increased proteoglycans throughout the valve, and

---

CLINICAL PERSPECTIVE

What Is New?

- This is a study on the role of pathologic mechanical tension on the papillary muscle from a prolapsing valve and how this abnormal valve motion induces regional fibrosis.
- Computational modeling paired with molecular, immunologic, and genetic studies indicate mechanosensory nodes that are abnormally stimulated in response to increased mechanical stress in fibrotic development.

What Are the Clinical Implications?

- These studies raise the question whether surgical intervention on patients with mitral valve prolapse should occur earlier than indicated by current guidelines to prevent advanced left ventricular fibrosis and potentially reduce residual risk of left ventricular dysfunction and sudden cardiac death.
- More research is needed that includes the marriage of enhanced imaging techniques with genetic and cellular mechanosensing mechanisms to understand initiating and sustaining signals driving regional fibrosis in patients with mitral valve prolapse.

Nonstandard Abbreviations and Acronyms

α-SMA	α-smooth muscle actin
CF	cardiac fibroblast
ECM	extracellular matrix
HCF	human cardiac fibroblast
KI	knock-in
PM	papillary muscle
WT	wild-type

collagen and elastin fragmentation. Disruption of these extracellular matrix (ECM) components, combined with valve interstitial cell hyperplasia, results in tissue enlargement and mechanical incompetence with leaflet billowing, malcoaptation, and chordal stretching and rupture.[3]

There is growing recognition that pathologic changes in MVP are not limited to the valve but commonly include myocardial fibrosis, which is associated with arrhythmias, sudden cardiac death, and potential for postrepair ventricular dysfunction.[4–6] Lethal left ventricular (LV) arrhythmias have been reported in association with inferobasal LV and papillary muscle (PM) fibrosis.[2,7,8] These findings were further supported by studies that found increased fibrosis in patients with ventricular arrhythmias,[8–10] and cardiac magnetic resonance imaging demonstrates regional LV fibrosis is more prevalent in MVP than patients without MVP with mitral regurgitation.[8,10,11] Furthermore, Basso et al and other groups have described fibrosis in patients with MVP as a potential arrhythmogenic substrate and plausible cause for sudden cardiac death in a subset of these patients.[2,12] The location of fibrosis and PM involvement suggest a relationship to localized LV stresses exerted by abnormal valve motion. How and if these stresses are translated into molecular and cellular changes within the LV wall to drive reactive fibrotic responses is unknown but would likely invoke mechanosensors on various cell types within the myocardial wall. Of potential relevance, genetic studies identified mechanosensing primary cilia as prominently involved in human MVP[13,14]; however, whether these cellular appendages can transmit altered mechanical stresses from a prolapsing valve to reactive changes in the LV remains to be determined.

To date, LV histopathology in patients with MVP as well as application of appropriate models to study mechanisms underlying potential regional LV fibrosis have been lacking. In this study we provide histopathological, cellular, and molecular evidence for profound regionalized LV fibrosis in a sample of patients with MVP undergoing surgical repair. To establish a platform for studying fibrosis mechanisms and potential therapies in MVP, a genetically and phenotypically accurate murine model of MVP ($Dzip1^{S14R/+}$) was evaluated.[13] In this model, we tested the hypothesis that myocardial fibrosis in MVP is progressive and has comparable location as well as histopathologic and molecular characteristics similar to patients undergoing mitral valve surgery. Computational models and validation in vitro revealed mechanosensory molecular nodes that promote fibrosis proportional to stress, consistent with the valve-related location of myocardial fibrosis. Our data demonstrate that regionalized LV fibrosis is a conserved process across species and involves a localized mechanomolecular response to sense and increased chordal tension from a prolapsing mitral valve.

METHODS

Materials Disclosures

The data that support the findings of this study are available from the corresponding author upon reasonable request.

Patient Consent and Recruitment

All procedures performed in the studies involving human participants were in accordance with the ethical standards of the institutional and national

research committee and with the 1964 Helsinki Declaration and its later amendments or comparable ethical standards. The study protocol was approved by the local ethics committee (study protocol number 450/18-ek), and informed written consent was obtained from each patient before study enrollment. Patients (n=6) with severe mitral regurgitation secondary to MVP and indications for mitral valve repair[15] were enrolled in the study. Exclusion criteria consisted of other possible causes of myocardial fibrosis including coronary artery disease, nonvalvular cardiomyopathy, aortic stenosis, and previous cardiac surgery. Patients underwent transthoracic and transesophageal echocardiography to confirm the cause of the MVP and assess LV function before surgery (Table S1). Cardiac magnetic resonance imaging, using T1 mapping before and after gadolinium contrast to calculate extracellular volume fraction and assess regional tissue abnormalities, as well as late gadolinium enhancement, was performed in all patients. Extracellular volume values for each patient were as follows: patient 1: 28.1%, patient 2: 31.8%, patient 3: 28.0%, patient 5: 25.9%, patient 6: 33%. Patient 4 stopped his CMR study before meaningful images could be obtained. During mitral valve repair surgery, biopsies were obtained from the inferobasal myocardium between the PMs in all patients (n=6), with biopsies of the interventricular septum (n=3) or LV apex (n=3) to serve as within-patient controls. Biopsies were obtained with a scalpel with a mean size of 84±71 mg SD. All samples were processed for pathology and immunohistochemistry.

Mouse Model of Nonsyndromic MVP

A single missense mutation in the *DZIP1* gene was identified as disease-causing in a large family with nonsyndromic MVP. This mutation was introduced into mice through CRISPR (clustered regularly interspaced short palindromic repeats)-Cas9 (CRISPR-associated protein-9) (designated *Dzip1$^{S14R/+}$*), and the knock-in (KI) mutant mouse was validated as having myxomatous mitral leaflets and functional MVP by echocardiography at 6 months of age, as described previously.[13] All animal experiments were performed under protocols approved by the Institutional Animal Care and Use Committees at the Medical University of South Carolina (Protocol No. 170092). Before cardiac resection, mice were anesthetized by a 1-time inhaled dose of 10 mL isofluorane (Piramal) for 1 minute in a closed chamber. Toe pinch confirmed deep anesthesia, and the method of euthanasia was cervical dislocation in accordance with the *Guide for the Care and Use of Laboratory Animals* (National Institutes of Health publication No. 85–23, revised 1996). Hearts were removed following cervical dislocation.

Histopathology and Immunohistochemistry

Masson's trichrome stain was performed on 5-μm paraffin-embedded sections from surgical biopsies of patients with MVP (n=6). Sections were deparaffinized and rehydrated through a graded series of 100%, 95%, and 70% EtOH and washed in distilled water. Samples were refixed in Bouin's solution for 1 hour at 56 °C and rinsed in running water. Sections were then stained in Weigert's iron hematoxylin solution (10 minutes), washed in water, stained in Biebrich scarlet-acid fuchsin (15 minutes), and washed in water. Samples were placed in phosphomolybdic-phosphotungstic solution (15 minutes) and transferred to aniline blue solution (10 minutes). Samples were briefly washed in water and placed in 1% acetic acid solution (5 minutes) and washed, followed by dehydration (95% and 100% EtOH) and cleared in xylene before mounting.

Immunohistochemical and fluorescence stains were performed on 5-μm paraffin-embedded sections from surgical biopsies of patients with MVP (n=6) as well as *Dzip1$^{S14R/+}$* KI MVP mice[13] and control wild-type (WT) littermates (*Dzip1$^{+/+}$*) at 2 months (KI: n=3, WT: n=5), 4 months (KI: n=4, WT: n=4), 5 to 6 months (KI: n=4, WT: n=3), and ≥7 months (KI: n=5, WT=3) of age, as previously described.[13,16–20] Primary antibodies and their dilutions included: acetylated tubulin (Sigma; No. T6793, 1:500), α-smooth muscle actin (α-SMA) (Sigma; No. A2547, 1:500), cluster of differentiation 206 (CD206) (R&D; No. AF2535, 1:100), cluster of differentiation 163 (Abcam; No. ab199402, 1:100), ADP ribosylation factor like GTPase 13B (ARL13B) (Protein Tech; No. 17711-1-AP, 1:500), and Collagen Telo (a generous gift from Dr. Stanley Hoffman; 1:250). Secondary antibodies (Invitrogen), used at a 1:100 dilution, included fluorophores 488, 568, and Cy5. Nuclei were stained with Hoechst (Life Technologies; No. H3569, 1:10 000). Slides were cover-slipped using SlowFade Gold Antifade Reagent (Invitrogen; No. S36936). Images were captured using a Leica TCS SP5 AOBS Confocal Microscope System and LAS AF version 2.6.3 build 8173 acquisition and analysis software, Zeiss Axioscope M2, or Olympus BH-2 brightfield microscope.

Statistical Analysis

Quantification of collagen content on immunohistochemical stains was performed in Adobe Photoshop CS6. For human biopsies, total pixel counts for collagen stains were obtained. Images from each of the experimental groups and anatomical locations were generated, and percent collagen content in each region was calculated. For the human biopsies, 6 equal surface area measurements were obtained for collagen expression per patient. Percentages were

calculated based on collagen pixel intensity divided by total pixel intensity. These 6 measurements were averaged to generate percent SEM. A similar approach was performed for mouse collagen fraction with minor modification. Papillary, peripapillary, and apex (control) regions were selected, and pixel intensity for collagen was obtained and divided by total pixels within each field. This generated a percent collagen fraction, which is graphically depicted by showing total percent collagen (fibrosis) within the papillary region and apex control tissue across multiple mice at varying ages (control WT littermates [*Dzip1*$^{+/+}$] at 2 months [KI: n=3, WT: n=5], 4 months [KI: n=4, WT: n=4], 5 to 6 months [KI: n=4, WT: n=3], and ≥7 months [KI: n=5, WT: n=3]). To assess normality of the data, a Shapiro-Wilk test was performed for each group of samples. For data that were normally distributed, a parametric test was used; when data were not normally distributed, a nonparametric test was used. For individual patient comparisons, a nonparametric Mann-Whitney *U* test was used to test for statistical changes in percent collagen fraction between either septum and papillary biopsies or apical and papillary biopsies, depending on which samples were available per patient. To compare the average percent collagen fraction of apical and septal biopsies with PM biopsies across multiple patients, a Student *t* test was used, because data were determined to be parametric. To compare the average percent collagen fraction for remote myocardium, which includes apical and septal samples depending on what was available per patient (n=6), compared with papillary myocardium (n=6), a Student *t* test was used because the data were normally distributed. For mouse analyses, to compare percent collagen fraction across different time points, a 1-way ANOVA was used with post hoc analysis using Dunn multiple comparisons test with the mean of the 2-month time point used as a referent control. To compare collagen fractions between control and *Dzip1* KI mice over time, we used a 2-way ANOVA, with post hoc testing using Bonferroni multiple comparisons test. For all analyses, an * indicates *P*<0.05, whereas ** and *** indicate *P*<0.01 and 0.001, respectively. Having 6 collagen measurements of each biopsy type (remote, papillary) per patient provided 80% power to detect large within-patient differences in collagen fractions between biopsy types (eg, Cohen *d* effect sizes equivalent to 1.8 SD units), as well as large differences (*d*=1.4) in average collagen fractions between biopsy types across all 6 patients, assuming 2-sided hypothesis testing and α=0.05. Only large differences (*d*=3–4, depending on whether data from 5 or 6 patients were available) were detectable between the patient subgroups with 80% power.

Quantification of α-SMA was performed by comparing pixel intensity within 6 representative fields. Quantification of CD206 was generated by counting total number of positive cells within 6 representative fields. Data are shown as fold-change in CD206 cell numbers between experimental and controls and percent of CD206 cells within particular regions. Total cells analyzed are presented in the figures. To detect statistically significant differences between test groups with 2-sided α=0.05, a Student *t* test was used.

Computational Modeling

To help identify potential signaling connections between mechanical tension and regional fibrosis, we adapted a previously published computational model of cardiac fibroblast (CF) signaling pathways.[21,22] This model captured the activity levels of 109 signaling molecules and 174 reactions connecting biochemical and mechanical input stimuli (mechanical tension, transforming growth factor beta 1, angiotensin II, interleukin 1, interleukin 6, platelet-derived growth factor, tumor necrosis factor alpha, endothelin 1, norepinephrine, and natriuretic peptide) to predict fibrosis-related outputs (collagen I, collagen III, fibronectin, periostin, α-SMA, matrix metalloproteinases, tissue inhibitors of metalloproteinases, and others). In the present study, we integrated an additional 27 new signaling molecules and 50 new network reactions related to cilia signaling that were manually curated from existing literature reports (Tables S2 and S3). Reactions were added if 2 or more prior experimental results were found that confirmed each particular reaction in CFs or similar cell types. The word "reaction" here is a general term used in reference to all reactions between species in the network. For example, TGFβ ligand interacting with its receptor is a reaction within the network. Our modeling approach simulated each reaction as a logic-based ordinary differential equation, wherein each molecule's activity is represented as a fractional value between 0 (fully off) and 1 (fully saturated), calculated from upstream input nodes using Hill-type sigmoidal ordinary differential equations and the associated reaction logic (ie, activation, inhibition, coactivation). Simulations of the CF signaling network and construction of ordinary differential equations were completed using Netflux software in MATLAB (MathWorks), as previously described.[22] In our past modeling studies, this model has successfully predicted ≈82% (96/118) of previously reported signaling responses by CFs under a wide variety of biomechanical and biochemical stimulation conditions.[21,22] Importantly, these validation agreements are based on >100 independent experimental studies, not including the ≈300 experimental studies used to build the model. In the current study, we investigated the connection between mechanical tension, cilia signaling, and downstream collagen production. For the tension dose-response simulations, tension stimulation was applied at increasing intervals of 10%

activation from 0% to 100% until species steady-state activation levels were achieved (11 total simulations). Biochemical input nodes were initialized at 10% activation to replicate basal activation of the CF. All other noninput nodes were initialized at 0% activation. The condensed network reconstruction and species heatmap were based on the steady-state species activation levels derived from these simulations.

Cell Culture and Western Analyses

Human CFs (HCFs) (Cell Applications) were cultured on substrates of increasing elastic moduli to interrogate the effects of ECM stiffness on HCF primary cilia. CytoSoft (Advance BioMatrix, Cat. No. 5142-5) collagen-coated silicone hydrogels were used with elastic moduli resembling normal working myocardium (8 kPa) compared with pathological conditions (16, 32, and 64 kPa).[23] HCFs were seeded at a density of 3×10^5 in 6-well CytoSoft plates in triplicate and allowed to reach near confluence over 48 hours. HCF-specific growth media were used for all plates (Cell Applications; 315-500). At 48 hours, HCFs were released from the silicone hydrogels using trypsin-EDTA, and protein lysate was collected. Western blot analysis of this protein lysate was conducted in triplicate and probed for the ciliary axoneme marker Arl13b (Proteintech; Cat No. 17711-1-AP). Goat-HRP secondary antibodies were used to detect Arl13b followed by West-Femto chemiluminescence detection reagent (ThermoFisher). Band intensities were calculated as described above and normalized against total protein loading via Ponceau S stain.

In addition, human cardiac fibroblasts were cultured in a 16-well silicone plate coated with 150 μL of collagen type 1 (3.37 mg/mL; Corning) at a seeding density of 2.5×10^4 per well. These cells were then subjected to either 10% mechanical strain (frequency 1 Hz) or 0% strain (static control) using a MechanoCulture FX plate stretcher (CellScale) for 24 hours. Following stretch, cells were lysed using RIPA buffer containing 1× Halt protease and phosphatase inhibitors cocktail (ThermoFisher) to extract proteins. To detect statistically significant differences between test groups with 2-sided α=0.05, a Student t test was used.

RNA Sequencing

Total RNA was isolated from the cells using the RNeasy Mini Kit (Qiagen), and RNA quality was determined using a nanodrop spectrophotometer (ThermoFisher). For each sample, 2 μg of total RNA were used in Illumina's TruSeq Stranded mRNA Library Kit (Cat No. 20020594). Libraries were sequenced on Illumina NextSeq 500 as paired-end 42-nt reads. Sequence reads were analyzed with the spliced transcripts alignment to a reference alignment–DESeq2 software pipeline. For read mapping, the paired-end 42 bp

sequencing reads generated by Illumina sequencing were mapped to the genome using the spliced transcripts alignment to a reference algorithm with default settings. Alignment information for each read is stored in the binary alignment map format. For fragment assignment, the number of fragments overlapping predefined genomic features of interest (eg, genes) were counted. Only read pairs that have both ends aligned were counted. Read pairs that have their 2 ends mapping to different chromosomes or mapping to the same chromosome but on different strands were discarded. The gene annotations used were obtained from the Subread package. These annotations were originally from the National Center for Biotechnology Information RefSeq database and then adapted by merging overlapping exons from the same gene to form a set of disjoint exons for each gene. Genes with the same Entrez gene identifiers were also merged into 1 gene. For differential analysis, after obtaining the gene table containing the fragment counts of genes, differential analyses to identify statistically significant differential genes using DESeq2 were performed. The following lists the preprocessing steps before differential calling: (1) Data normalization: DESeq2 expects unnormalized count matrix of sequencing fragments. The DESeq2 model internally corrects for library size using their median-of-ratios method. The gene table obtained from analysis step 2 is used as input to perform the DESeq2's differential test. (2) Filtering before multiple testing adjustment: After a differential test has been applied to each gene except the ones with zero counts, the P value of each gene is calculated and adjusted to control the number of false positives among all discoveries at a proper level. During this process, DESeq2 by default filters out statistical tests (ie, genes) that have low counts by a statistical technique called independent filtering. It uses the average counts of each gene (ie, base mean), across all samples, as its filter criterion, and it omits all genes with average normalized counts below a filtering threshold from multiple testing adjustment. This filtering threshold is automatically determined to maximize detection power (ie, maximize the number of differential genes detected) at a specified false discovery rate. (3) Differential calling: Differential genes are detected by DESeq2 at 0.1 (or 10%) false discovery rate (ie, adjusted P value). (4) Gene set enrichment analysis: Using DESeq2 normalized gene counts, we performed gene set enrichment analysis with default settings to determine whether members of an a priori defined gene set based on biological knowledge (eg, genes sharing the same gene ontology category) are enriched. Before running the gene set enrichment analysis, we add a small pseudocount to the normalized counts to avoid dividing by0 errors. Our standard gene set enrichment analysis uses MSigDB's C5 (gene ontology gene set) collection.

AdvaitaBio was also used as an efficient tool to prioritize differentially expressed gene pathways.

RESULTS

Surgical Patients With MVP Display Regional Fibrosis

Clinical information on the 6 patients with MVP can be found in Table S1. Sample preoperative transesophageal echocardiography (Videos S1 and S2) and cardiac magnetic resonance videos (Videos S3 and S4) are shown in supplemental files. Still images of 3-dimensional and 2-dimensional echocardiography show prominent posterior leaflet prolapse (Figure 1A and 1B). Patients typically had evidence of gross myocardial fibrosis in the PMs and surrounding inferobasal myocardium as determined by late gadolinium enhancement cardiac magnetic resonance (Figure 1C) and upon intraoperative visual inspection, with less/absent fibrosis in the interventricular septum and apex (Video S5). Successful mitral valve repair was performed via a minithoracotomy approach in all patients without any significant perioperative complications.

Biopsies of the 6 patients were obtained from the inferobasilar (peripapillary) region, where gross fibrosis was typically observed during surgery (Video S5). Additional samples from each patient were harvested from either the interventricular septum or the apex of the heart to serve as within-person controls. Masson's trichrome stain revealed pronounced replacement fibrosis within the inferobasal myocardium, with little evidence of fibrosis within the apex or interventricular septum (Figure 2 and Figure S1). Immunohistochemistry (IHC) confirmed a statistically significant increase in collagen type I protein in these fibrotic regions (Figure 2). Within the scar regions, myocyte loss was evident by both Masson's trichrome and IHC stains, and myocytes bordering the fibrotic zone displayed qualitative changes in cell size and presence of disorganized sarcomeres by IHC (Figure 2 and Figure S2). Those patients who displayed more pronounced fibrosis by IHC and Masson's trichrome stains (patients 2 and 6) also had more diffuse prolapse (P1, P2, P3 segments in patient 2 and bileaflet involvement in patient 6) (Figure S1). Although all biopsied patients showed substantial localized LV fibrosis, echocardiographic data did not reveal overt LV dysfunction (Table S1). Taken together, these histological and molecular data confirm regional LV fibrosis at the time of surgery in patients with MVP with nonischemic disease.

Regional LV Fibrosis Correlates With Myofibroblasts and Inflammation

Myofibroblast activity and inflammation have previously been correlated with fibrosis in numerous disease states. Thus, IHC was used to quantify whether molecular markers that demarcate these cell types correlated with the regional fibrosis observed in the LV surgical biopsies. High magnification of the fibrotic region in the peripapillary zone revealed numerous cells that stained for α-SMA, a marker for activated myofibroblasts (Figure 3). α-SMA–positive cells were also observed within the apex of the myocardium but were restricted, as expected, to small blood vessels and therefore do not represent activated fibroblasts (arrowheads in Figure 3A). Quantification of pixel density revealed a statistically significant increase in α-SMA within the fibrotic zone compared with remote myocardium (Figure 3B). As previous reports have demonstrated a role for innate immune cells in both initiating and contributing to fibrotic events in the heart,[23–27] we assayed whether macrophage markers were also uniquely present within these collagen-rich regions. As shown in Figure 3C and Figure S3, CD206- and cluster of differentiation 163-positive macrophages were abundant within the fibrotic zones. Quantification of CD206+ cells
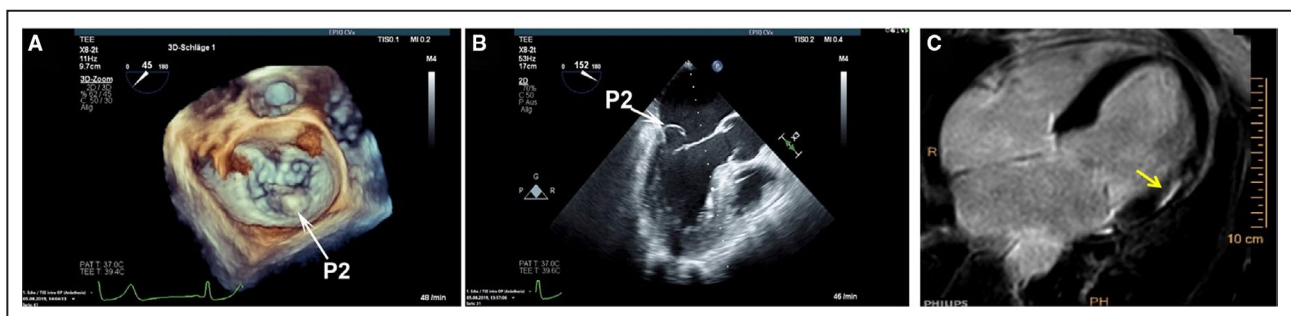
Figure 1. **Echocardiographic visualization of mitral valve prolapse (MVP) and associated left ventricular (LV) fibrosis.**
A and **B**, Three-dimensional and 2-dimensional transesophageal echocardiography MVP showing prolapse of the P2 segment (white arrows). **C**, Cardiac magnetic resonance with late gadolinium enhancement showing evidence of inferobasal LV fibrosis underlying the papillary muscles (yellow arrows).
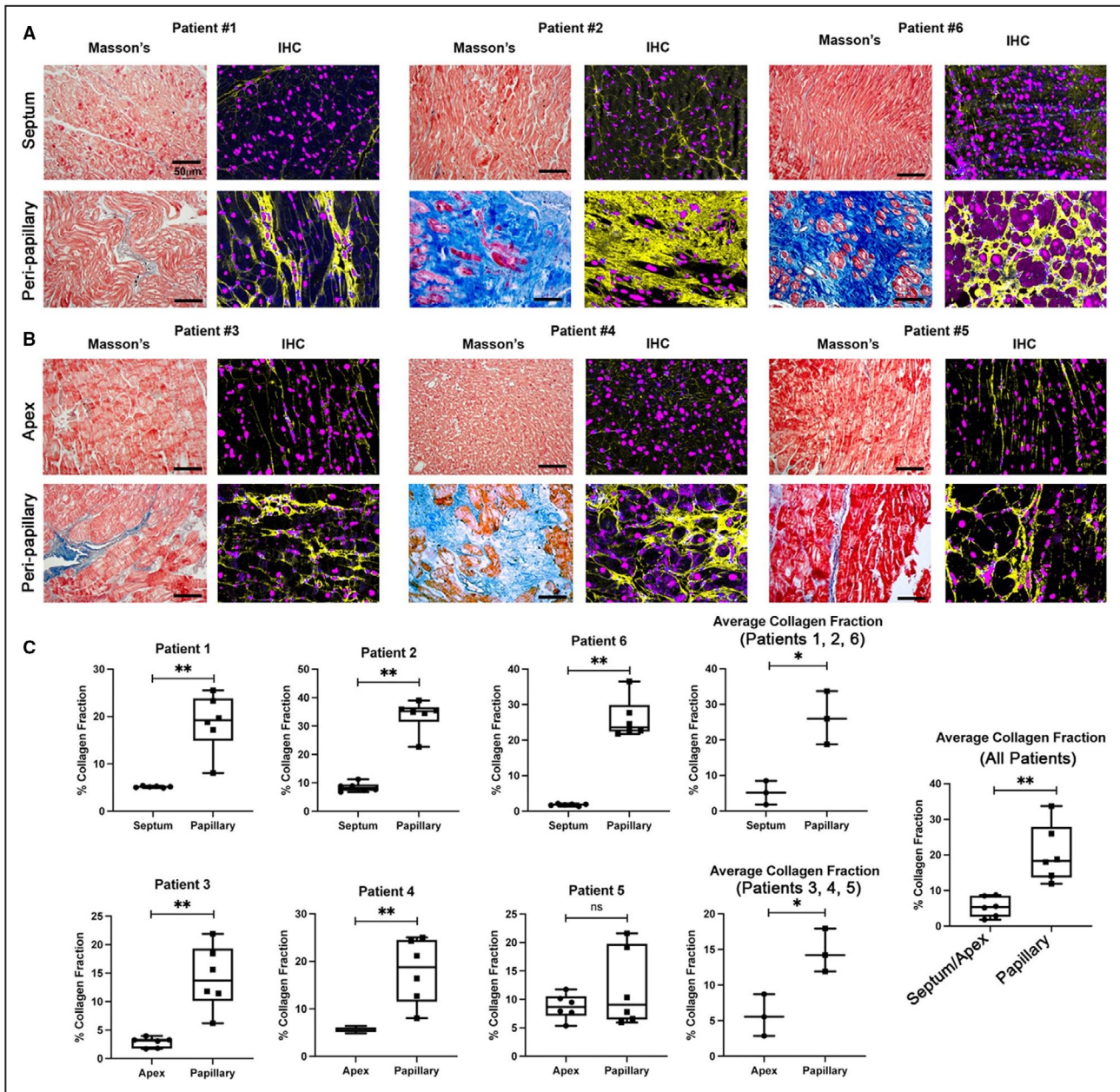
Figure 2. Regional left ventricular (LV) fibrosis in human patients with mitral valve prolapse (MVP).

Masson's trichrome and immunohistochemistry (IHC) for collagen (yellow) shows prominent LV fibrosis in the peripapillary region of surgical mitral valve repair patients compared with either septal (**A**) or apex (**B**) biopsies. **C**, Quantification of fibrosis shows significant elevation of collagen I protein in peripapillary regions compared with either septal or apex in-person control tissue. Amounts are shown as percent collagen fraction (positive pixel staining/total pixels). Zones of myocyte loss are evident, indicating replacement fibrosis. Scale bars=50 µm. Blue=collagen histological (Masson) stain, red=myocytes histological (Masson) stain, purple=nuclei (Hoechst). *P<0.05, **P<0.01.

revealed a 3-fold increase in macrophages when comparing peripapillary region to apex and a 5-fold increase when compared with septal myocardium (Figure 3D). The total average percentage of CD206+ cells within the peripapillary region was ≈25% (N=826 cells) compared with ≈5% within the septum (N=586 cells) or apex (N=502 cells). These data demonstrate that activated myofibroblasts and inflammation are associated with regional LV fibrosis in patients with MVP.

Regional LV Fibrosis Is Conserved Across Species

In our previously reported mouse *Dzip1^S14R/+* model for nonsyndromic MVP, 100% of mice with the human
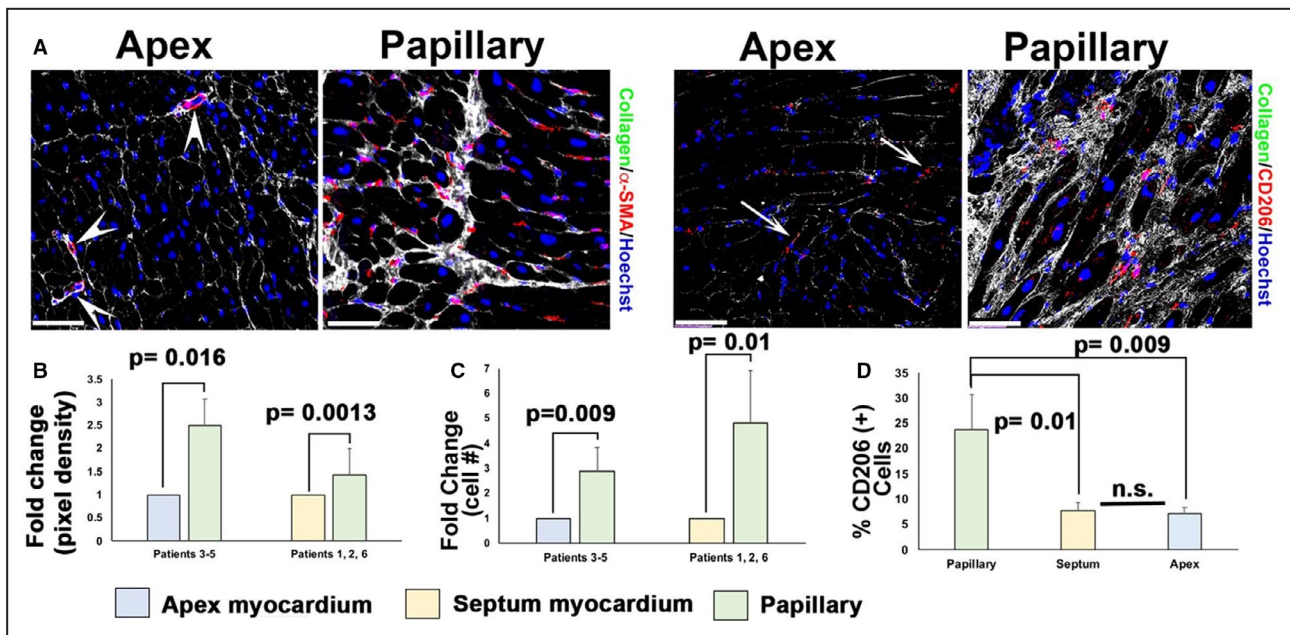
Figure 3. Fibrosis in patients with mitral valve repair correlates with activated cell types specific to peripapillary regions. **A**, Immunohistochemistry (IHC) (white arrows, purple staining) shows increased α-smooth muscle actin (α-SMA) and cluster of differentiation 206 positive (CD206+) macrophages within fibrotic areas (white, collagen) localized to peripapillary regions (arrows) of the left ventricle compared with in-person apex tissue. Scant α-SMA+ cells within capillaries are observed in apex tissue (arrowheads in **A**), and few macrophages are present within the apex (arrows). **B** through **D**, Quantification of IHC data shows 2- to 3-fold increase in α-SMA expression, a 3- to 5-fold increase in cluster of differentiation 206 (CD206) macrophages, and ≈25% total CD206+ cells within the fibrotic peripapillary region compared with apex or septal in-person control tissues. Scale bars=100 μm.

mutation developed myxomatous valves and functional MVP by around 6 months of age.[13] To determine whether *Dzip1*[S14R/+] mice also develop regionalized fibrosis, we conducted similar stains as in the human biopsies. For consistency of analysis, we performed IHC initially on the exact *Dzip1*[S14R/+] and control mice that were previously reported as having myxomatous valves and functional MVP at 6 months of age.[13] As shown in Figure 4, *Dzip1*[S14R/+] mice show significant elevation of collagen I in both the inferobasal wall (Figure 4A through 4C) and PM (Figure 4D and 4E) compared with age-matched WT control animals. We also observed robust increases in both α-SMA and CD206 staining, demonstrating activated myofibroblasts and macrophage presence within the fibrotic papillary and inferobasal LV. These activated cell types were largely absent from the same regions in control animals. Consistent with our human data, these increases in collagen content, activated cell types, and macrophages were uniquely observed within the peripapillary and inferobasal myocardium and absent within myocardial apex tissue (Figure 4F).

LV Fibrosis in MVP Is Progressive

As our data demonstrated significant regional LV fibrosis in a validated nonsyndromic MVP mouse model, follow-up studies tested whether fibrosis with

collagen deposition progresses in *Dzip1*[S14R/+] mice at 2-, 4-, 5 to 6-, and ≥7-month time points. As shown in Figure 5, IHC shows that 2-month *Dzip1*[S14R/+] mice have low-level collagen expression that is comparable to control animals (*Dzip1*^{+/+}) (Figure 5A and 5E). By 4 months of age, collagen deposition becomes elevated within the PM and adjacent LV myocardium of *Dzip1*[S14R/+] mice compared with controls (Figure 5B and 5F). By 6 months of age, abundant collagen is observed throughout the PMs of the *Dzip1*[S14R/+] mice compared with controls (Figure 5C and 5G). At ≥7 months of age, control animals still have little detectable collagen (Figure 5D), whereas *Dzip1*[S14R/+] mice display pronounced fibrosis with globular zones of collagen accretion (Figure 5H). The highest level of collagen expression begins primarily at the PM tip at 4-months and then extends through the PM belly in a gradient fashion as the animals age. Quantification of collagen content by IHC revealed no statistically significant increase in collagen I protein expression in WT (*Dzip1*^{+/+}) control tissues as a function of age (Figure 5I). However, in the *Dzip1*[S14R/+] mice, significant elevation of expression is observed with time (1-way ANOVA P=0.0004) (Figure 5J). From 2 to 6 months of age, there was a trend toward increased collagen as seen in the IHC; however, this did not reach significance. Following 6 months of age, a time point in which we previously detected MVP in
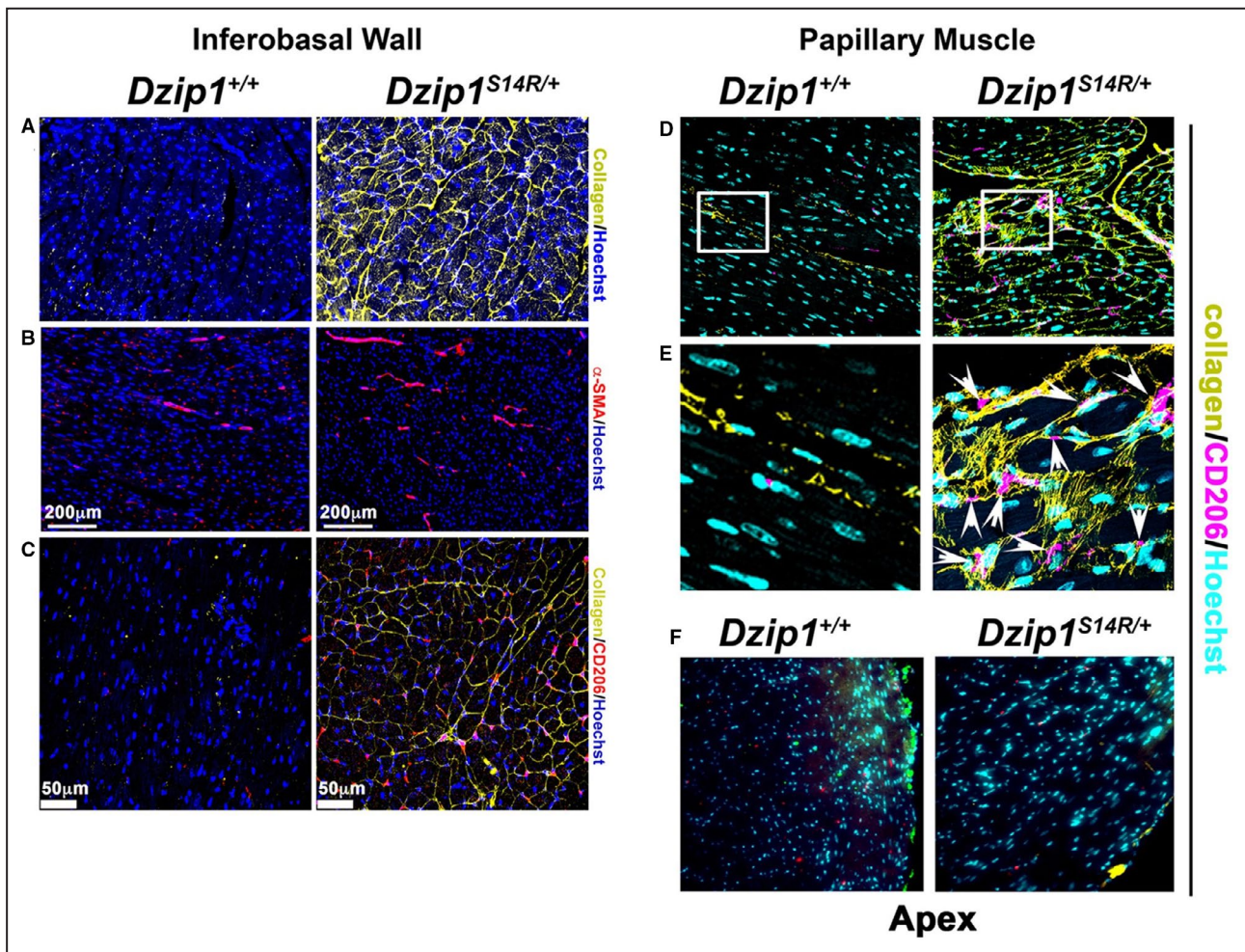
Figure 4. *Dzip1*^*S14R/+* **mitral valve prolapse mice have regionalized left ventricular (LV) fibrosis similar to human patients.**
Immunohistochemistry at 6 months showing regionalized LV fibrosis (collagen, yellow) within the inferobasal wall (**A** and **C**) and papillary muscle (**D**) that correlates with increased presence of α-smooth muscle actin (α-SMA⁺) (**B**) and cluster of differentiation 206 positive (CD206⁺) (**C** and **D**, arrow heads in **E**) cells compared with wild-type *Dzip1* mice (*Dzip1*^+/+^). Higher magnification of boxed regions in (**D**) are shown in (**E**). Activated cells were specific to fibrotic regions in *Dzip1*^*S14R/+* mice, because apex tissue from control and mutant animals did not reveal evidence of increased α-SMA or cluster of differentiation 206 (CD206) cells (**F**). Nuclei=blue (**A** through **C**), turquoise (**D** through **F**). Scale bar sizes are noted in the figure.

the *Dzip1*^*S14R/+* mouse,[13] we observed a significant increase in collagen deposition (Figure 5J). Expression of collagen continued to increase after this time point and was statistically significant from all previous time points studied. Comparison between the control and *Dzip1*^*S14R/+* mice for collagen within the posterior–medial papillary showed that *Dzip1*^*S14R/+* mice develop progressive fibrosis over time compared with control mice (2-way ANOVA *P* for interaction=0.004). Statistically significant increases for collagen for time points >6 months of age were identified (Bonferroni *P*<0.0001 at the 7+-month time point) (Figure 5K). These data highlight a regionalized and progressive accumulation of fibrosis within the PMs and inferobasal LV, and is consistent with MVP-driven mechanical tension as contributing to a progressive, regionalized fibrotic phenotype.

Computational Modeling Indicates Mechanical Tension as a Driver of Fibrosis

To probe a link between MVP and an LV fibrotic phenotype, we hypothesized that increased chordal tension from the prolapsing valve can promote CF activation in regions of increased stress. We applied a validated in silico model for how the CF responds to tension.[21,22] This model is based on our previously established computational model of the CF and uses a logic-based, ordinary differential equation modeling approach to provide insight into CF dynamics.[21,22]
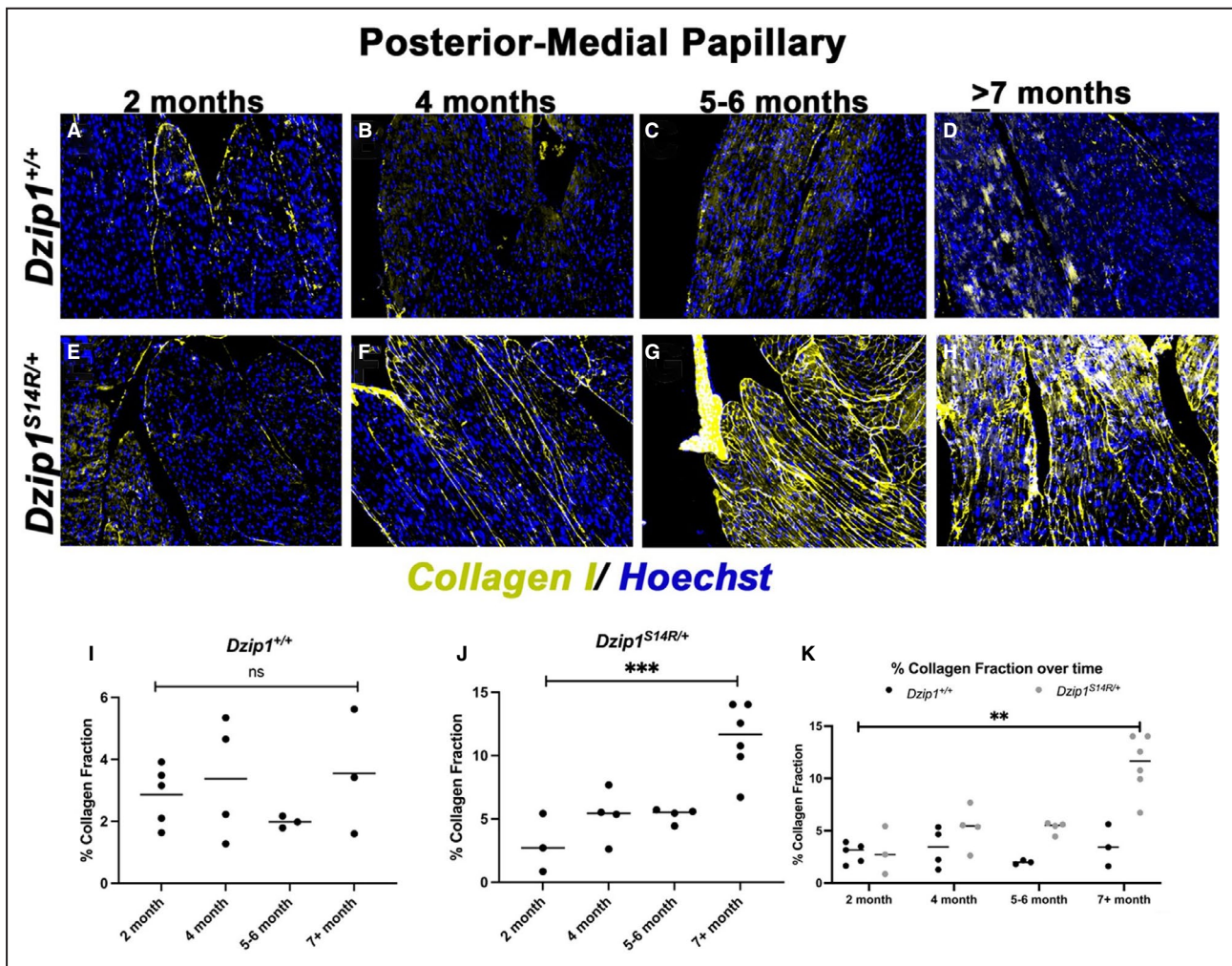
Figure 5. Regionalized fibrosis progression is observed in *Dzip1^{S14R/+}* mice.
A through **D**, Immunohistochemistry for collagen I (yellow) over time shows no discernible increase of collagen production within the posterior–medial papillary muscle of control mice (*Dzip1^{+/+}*). **E** through **H**, *Dzip1^{S14R/+}* mitral valve prolapse mice show increased collagen I staining (yellow) over time within the papillary muscle. **I**, Quantification of percent collagen fraction of tissue within the control papillary muscle shows no significant change in expression over time. One-way ANOVA resulted in a *P*=0.55. **J**, Compared with 2 months of age, the *Dzip1^{S14R/+}* posterior–medial papillary muscle shows a trend toward increased fibrosis by 5 to 6 months of age and ≈5-fold increase by ≥7 months. ***One-way ANOVA resulted in a *P*=0.0004. **K**, Compared with control animals, significant differences in collagen within the papillary muscle is observed in *Dzip1^{S14R/+}* mice (2-way ANOVA *P* for genotype=0.0005, *P* for time point<0.0001, *P* for interaction=0.004). Post hoc comparison of individual time points using Bonferroni multiple comparisons test found that significant differences in collagen are present by ≥7 months of age (*P*<0.0001), whereas a trend for increased collagen is observed by 6 months of age (*P*=0.12). ns, not significant; ***P*<0.01; ****P*<0.001.

This model was expanded to include a signaling network related to primary cilia activity and to integrate cilia signaling with mechanosensing signaling nodes. We included primary cilia in our analyses, because recent data have suggested a role for these mechanosensing cellular antennae in both MVP and cardiac fibrosis.[13,14,17,20,28,29] In addition, primary cilia have been previously shown to function in signal transduction pathways that are linked to collagen synthesis and deposition, including hedgehog, WNT/β-catenin, TGF-β, and cytoskeletal organization cascades.[30–38] Activation of these various signaling cascades were interrogated by assessing node activation patterns for well-characterized downstream effectors of these pathways (Figure S4). A condensed form of the CF network is shown with nodes relevant to fibrotic pathways (Figure 6A). CFs, in response to high-tension stimulation (tension activation=90%), showed a robust activation of profibrotic signaling pathways (Figure 6B). Next, we evaluated the activation of species directly related to the development of fibrosis. Expected increases in canonical and noncanonical TGF-β signaling as well as fibrosis-related transcription factors (myocardin related transcription factor, extracellular related kinase,
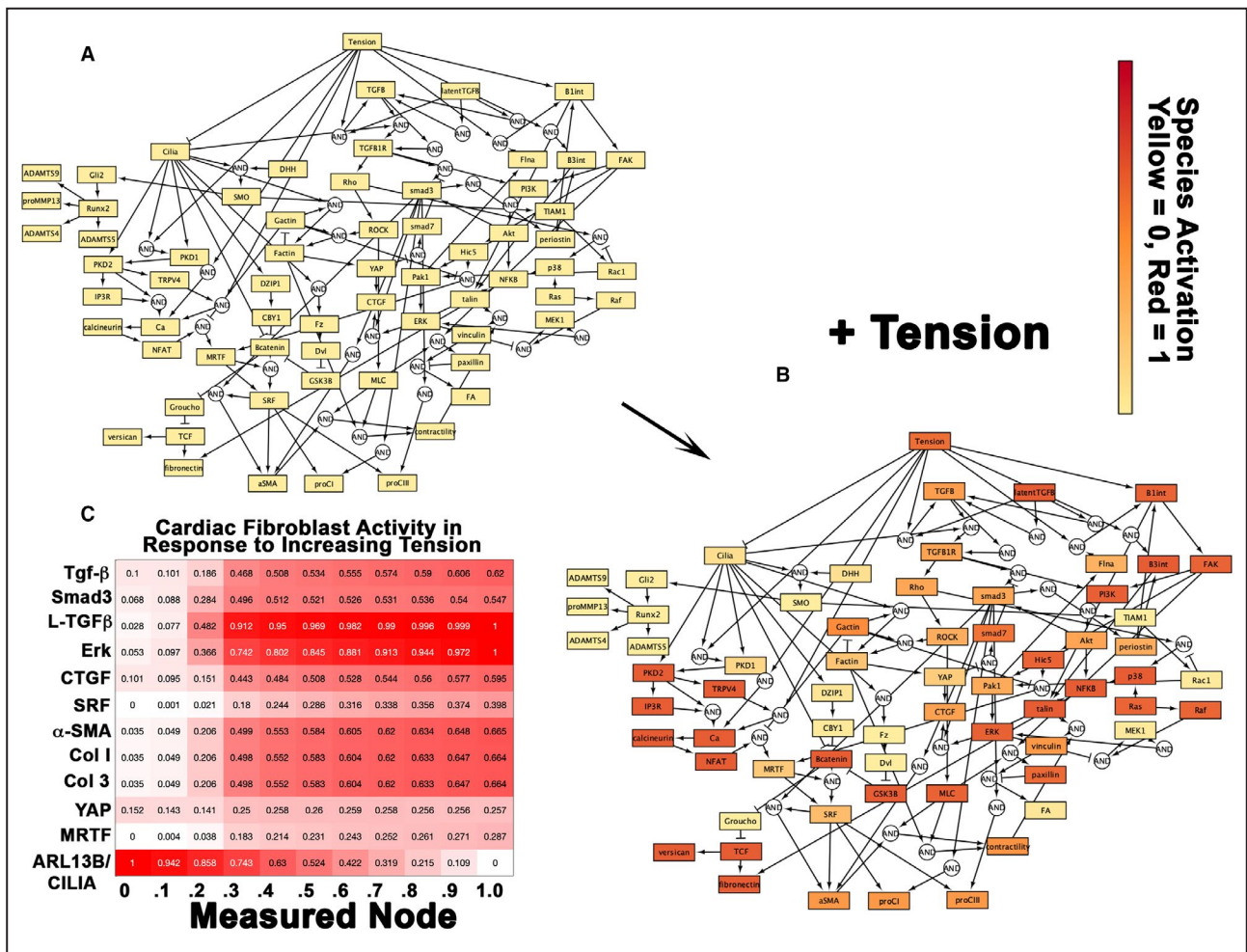
Figure 6. Predictive computational model of cardiac fibroblasts in response to tension indicates mechanosensory responses.

For the tension dose-response simulations, tension stimulation was applied at graduating intervals of 10% activation from 0% (static, **A**) to 100% (**B**) until species steady-state activation levels were achieved. The condensed network reconstruction (**A** and **B**) and species heatmap (**C**) were based on the steady-state species activation levels derived from these simulations. Cardiac fibroblasts, in response to high tension stimulation (tension activation=90%), showed a robust activation of profibrotic signaling pathways (**B** and **C**). Tension stimulation was integrated into the cardiac fibroblast (CF) signaling network dynamics through the primary cilia and β-integrin nodes. Expected increases in canonical and noncanonical TGFβ signaling as well as fibrosis-related transcription factors (myocardin related transcription factor [MRTF], connective tissue growth factor [CTGF], yes-associated protein [YAP], serum response factor [SRF], mothers against decapentaplegic homolog 3 [Smad3], extracellular related kinase [Erk]) are shown and are associated with increased collagen-1, 3, and α-smooth muscle actin (α-SMA) activity (**C**). A positive dose-response relationship is evident between the CF profibrotic response and tension stimulation but inversely related to primary cilia and ADP ribosylation factor like GTPase 13B (ARL13B) (**C**).

serum response factor, mothers against decapentaplegic homolog 3, yes-associated protein) are shown and are associated with increased collagen-1 and α-SMA activity (Figure 6B and 6C). Furthermore, a positive dose-response relationship is evident between the CF profibrotic response and tension stimulation. Additionally, we identified primary cilia as most responsive in areas of low tension, with a dose-dependent loss of these structures as tension increases.

To determine if there is a correlation between primary cilia and tension in vivo, we analyzed papillary and apex biopsies from surgical patients with MVP.

As shown in Figure 7A and 7B, in apical myocardium, under low/steady-state levels of mechanical tension, prominent ciliary axonemes are observed. However, in the peripapillary regions that show prominent replacement fibrosis, reduced axoneme staining is observed. Quantification of pixel intensities for acetylated tubulin revealed ≈6-fold reduction in staining in the fibrotic compared with nonfibrotic regions (Figure 7C). We further tested whether substrate stiffness impacts expression levels of ARL13B, a surrogate for axonemal biogenesis. As shown in Figure 7D and 7E, substrates with low elastic moduli
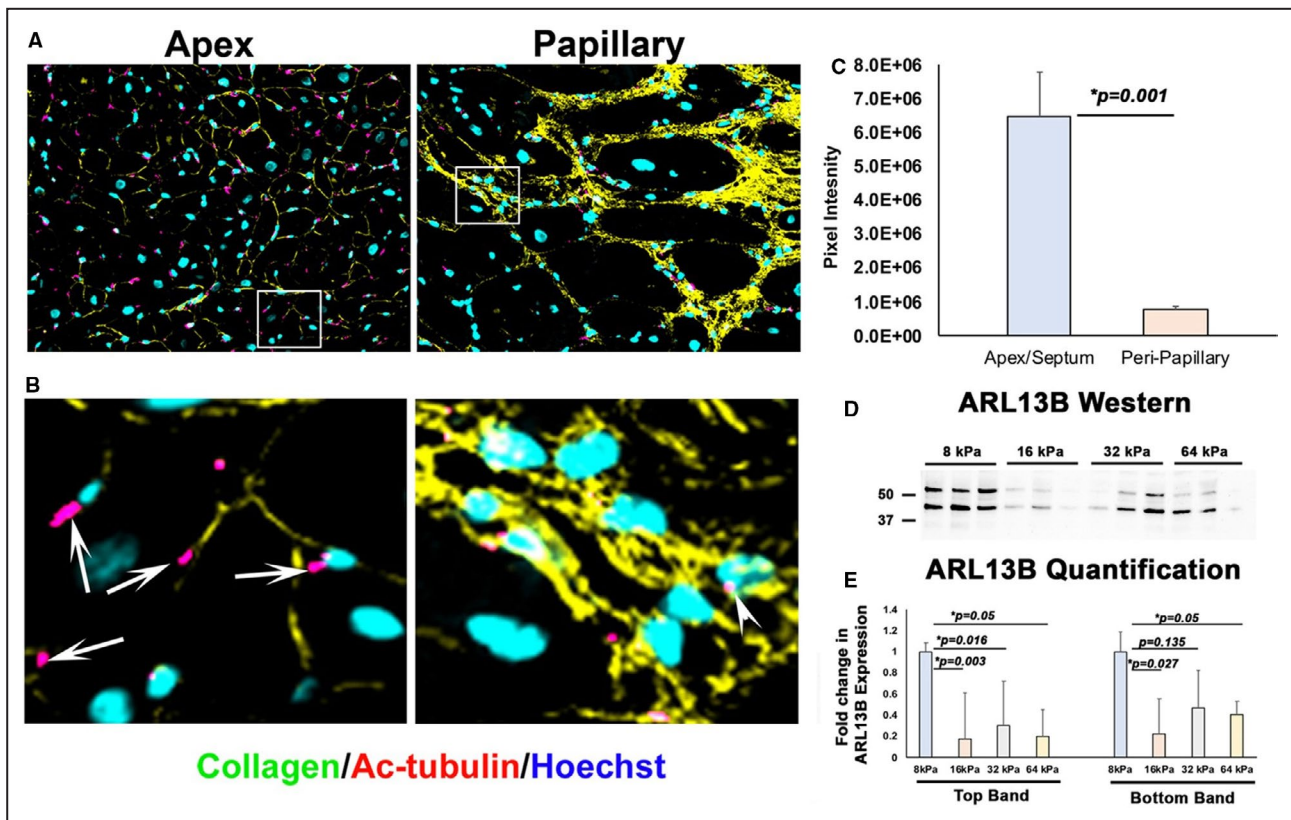
Figure 7. Primary cilia are deficient within human peripapillary fibrotic regions in patients with mitral valve prolapse.
A and **B**, Within apex myocardium of patients with mitral valve repair, primary cilia axonemes (pink) are evident (arrows). Within fibrotic zones of the peripapillary regions, axonemes are either absent or deficient as quantified by immunohistochemistry and pixel intensity (**C**). Western analyses of human cardiac fibroblasts plated on matrices of increasing stiffness showed a significant downregulation of ADP ribosylation factor like GTPase 13B (ARL13B) protein, a surrogate for primary ciliogenesis (**D** and **E**). Scale bars sizes are denoted in panels.

(8 kPa), which represent the mechanical environment of normal working myocardium, show robust expression of ARL13B. However, as the substrate increased in stiffness, as occurs during fibrosis, expression of ARL13B was significantly downregulated (Figure 7D and 7E). These in vivo and in vitro results validate our computational model prediction that increased mechanical tension can simultaneously lead to decreased cilia and increased fibrosis.

RNA Sequencing Identifies Tension-Driven Profibrotic Pathways

Our human, mouse, and in silico modeling data demonstrated fibrosis in areas of myocardium that experienced increased mechanical tension and suggested that tension drives fibrogenesis in MVP. To test this hypothesis, we performed mechanical stretch experiments on human cardiac fibroblasts. Following 24 hours of cyclical longitudinal strain (10%, 1 Hz), RNA sequencing identified 1761 transcripts that were nominally significant (adjusted $P<0.1$), of which 232 transcripts were statistically significant after correction

for multiple testing (adjusted $P<1.6\times10^{-6}$; Figure 8A, 8B and Figure S5). These 232 transcripts included collagens 1α1, 1α2, 4α1, 5α1, 5α3, 7α1, as well as proteins involved in translation initiation (eukaryotic translation initiation factor 4A2), posttranslational collagen assembly, trafficking, and processing, (prolyl 4-hydroxylase subunit alpha 1, prolyl 4-hydroxylase subunit alpha 2, prolyl 4-hydroxylase subunit Alpha 3, prolyl 3-hydroxylase family member 4, procollagen-lysine, 2-oxoglutarate 5-sioxygenase 2, and lysyl oxidase, and serpin family H member 1), and markers of fibroblast activation (actin alpha 2, smooth muscle). Conversely, proteolytic enzymes (matrix metalloproteinase 1 and a disintegrin and metalloproteinase with thrombospondin motifs 15) were downregulated (Figure 8B). Gene ontology analyses of cellular components using all nominally significant transcripts revealed 75 pathways that were statistically enriched following mechanical stretch. The most significantly different pathways corresponded to the extracellular space, secretory pathways such as vesicles and endosomes, and pathways relating to the cell membrane and cell–cell and cell–matrix adhesion (Figure 8C). To validate our
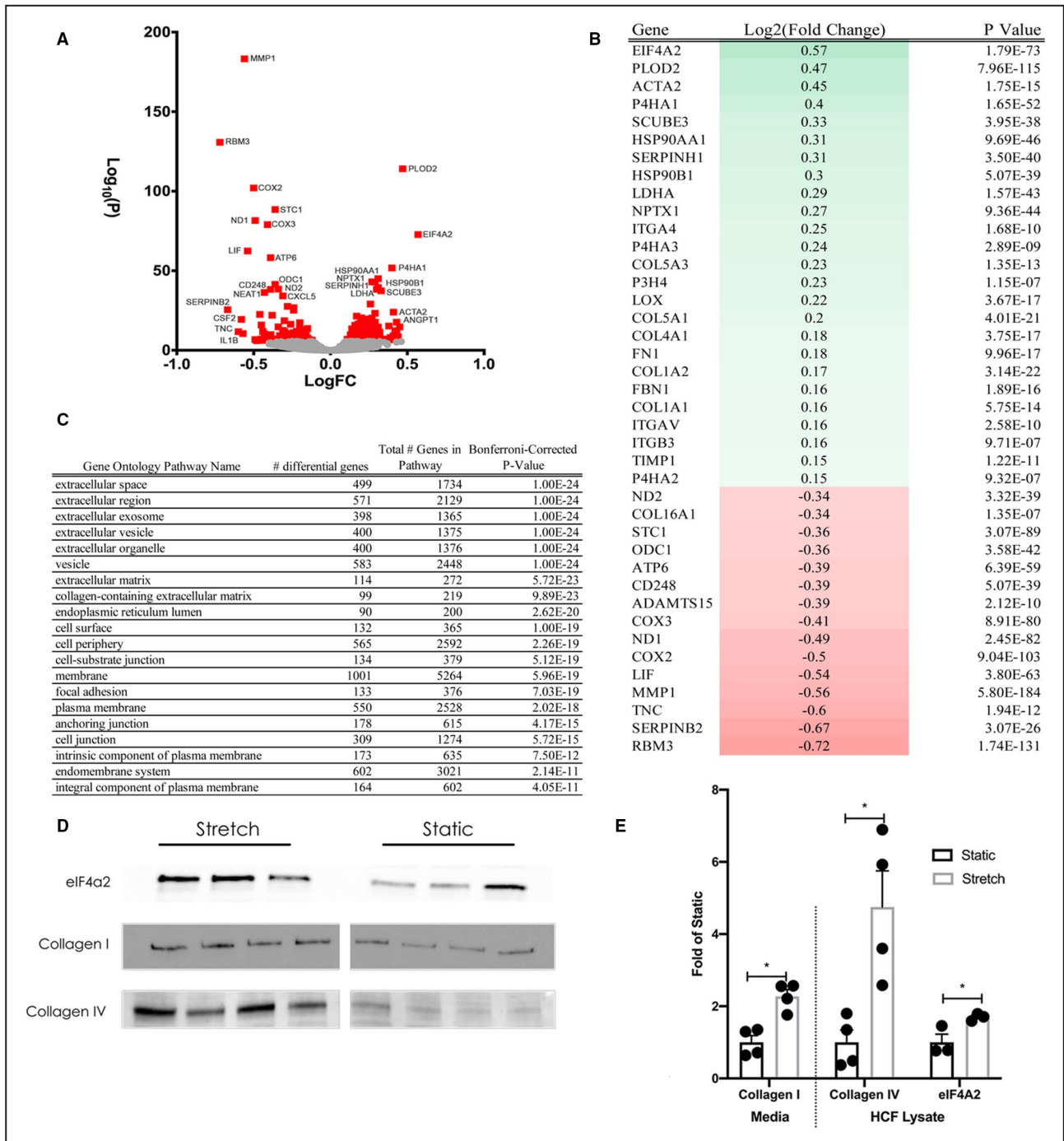
Figure 8. Cyclical stretch of human cardiac fibroblasts (HCFs) reveals tension responsive changes in extracellular matrix gene expression and protein production.
A, Volcano plot showing global changes in gene expression between stretched (10% longitudinal strain, 24 hours) vs static (0% longitudinal strain, 24 hours) HCFs. **B**, Heatmap of the top differentially expressed genes. **C**, Gene ontology analysis revealed that pathways corresponding to the extracellular space were enriched by mechanical stretch. **D** and **E**, Western blots performed on cell lysates and media from stretched and static HCF showed differences in collagen 1 protein in the media, and collagen IV and eukaryotic translation initiation factor 4A2 (eIF4A2) protein in cell lysates. FC indicates fold change. *$P<0.05$

computational model and RNA sequencing data sets, Western analyses were conducted on cell extract and media from stretched cells. Following 24 hours of mechanical stretch (10%, 1 Hz), proteins extracted from cell lysates showed increased production of eukaryotic translation initiation factor 4A2, an initiation factor in protein biosynthesis, and collagen type IV (Figure 8D and 8E). An increase in secreted collagen type I was

observed in the media from stretched cells compared with static (Figure 8D and 8E). These data confirmed that mechanical stretch of human ventricular cardiac fibroblasts enhances a fibrogenic response in vitro.

DISCUSSION

Our results show histological and molecular evidence for regional LV myocardial fibrosis in patients with MVP. Cross-species analyses in murine models validates a similarly localized, evolutionarily conserved fibrotic process observed in patients with MVP. Myofibroblast presence, inflammation, and fibrosis progression are predominantly localized to the inferobasal wall and attached PM that are physically and mechanically linked to the prolapsing leaflets. These data suggest an effect of valve-induced mechanical stresses through the chordae tendineae on interstitial cell biology and tissue-level responses. Lending additional support to this hypothesis, our studies show that profibrotic molecular changes can be reproduced in a validated computational model of fibroblast activation, as well as in in vitro models that apply biomechanical tension to cells. A colocalized presence of myofibroblasts and inflammation is consistent with previous reports of cardiac fibrosis, mostly in ischemic settings.[23–27] In that context, lack of blood flow induces cell death, a known potent nidus for early and prolonged inflammatory processes that initiate and propagate scar formation to prevent catastrophic cardiac rupture. Our studies show an inflammatory and activated cell phenotype response in the absence of ischemia in human and mouse MVP, and support the notion that changes in the mechanical environment are sufficient to engender reactive phenotypic and molecular responses that culminate in fibrosis.

How regionalized LV inflammation is activated in MVP is unknown. Based on the localization of inflammation and fibrosis, it is possible that mechanically induced cell membrane deformation results in release of proinflammatory cytokines, ions, and/or other small molecules (ie, ATP).[39] This effect is likely felt by all cell types within the affected areas, including fibroblasts, myocytes, endothelial cells, and resident inflammatory cells.[40,41] If various proinflammatory or profibrotic stimuli are released from these cells, or whether these stimuli act locally and/or systemically to induce/enhance inflammation are not known. Damage of stretched cell membranes may also induce cell death, which in turn would incite an innate inflammatory response initiated by neutrophils and propagated by macrophages. Although our data do not explicitly demonstrate that membrane stretch is inducing release of inflammatory attractants, cell death, and/or autophagy, we do show evidence of myocyte loss and subsequent replacement fibrosis in both human patients with MVP and our mouse model. Thus, myocyte loss, replacement fibrosis, and an altered mechanical environment may all be potent stimuli for continued inflammatory involvement necessary for scar progression. These molecular and cellular changes are only observed within regions of the LV that are tethered to the prolapsing valve through the chordae tendineae and PM, leading us to conclude that mechanical changes induced by a prolapsing valve likely drive phenotypic responses within the LV, independent of mitral regurgitant volume overload, although that can augment the process.[11] Recent studies have shown that isolated mitral regurgitation without MVP has a much smaller effect on magnetic resonance imaging–indicated fibrosis than MVP.[11]

Transmission of excess force by a prolapsing valve will likely be felt by various mechanonsensors within tissue and cells that are tethered to these excess forces within the PM and inferobasal myocardium. The primary cilia serve as cellular antennae that respond to these forces within the LV myocardium. Cell membrane tension on the primary cilia will affect all functional aspects of their mechanosensing.[42,43] Recent studies have invoked mechanosensing primary cilia as involved in ECM production and/or fibrotic diseases. Profibrotic molecules such as TGFβ have been shown to suppress ciliogenesis through negative regulation of the essential ciliogenic gene, *Ift88,* and knockdown of *Ift88* enhances TGFβ-induced collagen expression.[44] This finding of enhanced collagen synthesis during impaired ciliogenesis is consistent with recent data from multiple groups in ciliopathy patients who have mutations in critical ciliogenesis genes.[45] Human ciliopathy conditions, such as polycystic kidney disease, Bardet-Biedl syndrome, and others, commonly have extensive fibrosis within affected organs. Knockdown of zebrafish polycystins, mechanosensitive receptors/channels localized to the primary cilium, induces substantial collagen type I overexpression.[46] Similar findings were obtained from our group in mitral and aortic valve studies showing that loss of ciliogenic genes results in a robust increase in ECM synthesis, including collagen type I.[13,17,20,31] Although clinical cardiovascular studies are limited relative to the function of primary cilia, one study has described loss of primary cilia correlated with increased fibrosis in biopsies from patients with atrial fibrillation.[47] In this same study, loss of primary cilia by RNAi in fibroblasts increased presence of myofibroblasts and expression of ECM genes in response to transforming growth factor beta 1.[47] Because the potential role of cilia in fibrosis is gaining increased attention, it is becoming more evident that mechanical stresses acting through these structures have an impact on fibrosis pathways. In this study, we show that primary cilia are present within normal adult working myocardium in humans but are deficient in areas of regional fibrosis in MVP biopsies. Although fibroblast

Model of stress-induced fibrosis in MVP
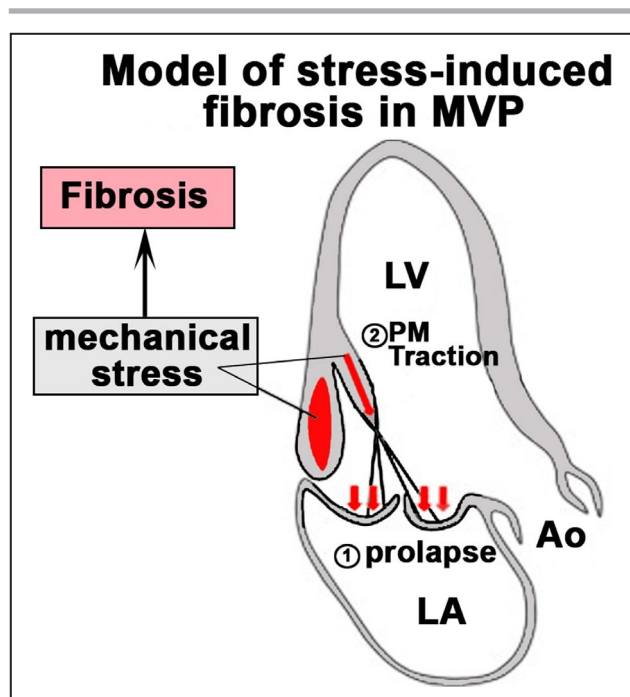
Figure 9.   Model for stress-induced fibrosis in mitral valve prolapse (MVP).
MVP (1) induces increased PM traction (2) and basal LV wall tension as fibrotic stimuli resulting in regionalized fibrosis (red). Ao indicates aorta; LA, left atrium; LV, left ventricle; and PM, papillary muscle.

primary cilia appear to be required for fibrosis suppression, our data also support a role for ECM stiffness as a suppressive ciliogenic signal as shown in Figure 7. Mechanical forces may stimulate a fibrogenic response regardless of any particular genetic mechanism or mechanosensor. Also worthy of consideration for future investigation are other stretch-activated signaling pathways associated with inflammation. Of these, those linked to mechanosensitive Cx43 (connexin 43) hemichannels may be of interest and relevance.[48,49] Release of purinergic signaling molecules by hemichannels such as ATP in response to disease, injury, or infection are a known activator of the innate inflammatory response.[50–52] Cx43 hemichannels have also recently emerged as key pathogenic determinants of myocardial fibrosis, in diseases such as arrhythmic right ventricular cardiomyopathy[53] and Duchenne muscular dystrophy.[54] Interestingly, Cx43 hemichannels have been localized on primary cilia in auricular chondrocytes where they are thought to function as a mechanosensitive ATP-release channel.[55]

Clinical Implications and Conclusions

MVP has been associated with LV remodeling, LV dysfunction, heart failure, arrhythmogenesis, and sudden cardiac death if left untreated.[7,56] Mitral valve repair is a highly effective therapy for severe mitral regurgitation because of MVP but often leaves patients with residual fibrosis and LV dysfunction and arrhythmias.[57] Our mouse models demonstrate that regionalized LV fibrosis in MVP is progressive and has a similar localization and molecular and cellular signature as in the human disease. The localization of fibrosis within the myocardium suggests a role for increased mechanical stress through the chordae in MVP (Figure 9), consistent with recent reports.[58–60] Support for increased mechanical stress is also based on a recent study that showed primary chordal forces, and therefore the force on the attached papillary muscles, are 5-fold higher in bileaflet prolapse compared with post–mitral valve repair.[61] Although our current findings and previous reports strongly support primary cilia defects in the cause of MVP, it is likely that MVP and MVP-associated LV remodeling do not solely stem from defects in the cilia pathway but instead through alternate independent mechanisms. Nonetheless, our computational modeling, which in turn is validated by molecular and cellular analyses in mouse and human MVP samples, further supports induction of fibrosis through increased mechanical stress. Waiting for traditional indications for mitral valve repair (ie, symptoms, LV dilation, LV dysfunction) may be associated with reduced survival after repair,[5] and therefore, identification of other important predictors of outcome (eg, advanced fibrosis) may have the potential to affect clinical guidelines and practice. Although no studies to date have unequivocally shown that earlier surgery leads to less fibrosis and sudden death, several studies have demonstrated better long-term survival if surgery is performed earlier in the disease process.[57] However, more and long-term data are required to link MVP-induced fibrosis with postoperative LV dysfunction and long-term mortality, which are beyond the scope of this study. Regardless, uncovering mechanisms of mechanical, cellular, and molecular changes within the left ventricle of patients with MVP, as shown in this study, may provide understanding of residual contractile dysfunction and electrical instability after mitral repair.

REFERENCES

1. Nkomo VT, Gardin JM, Skelton TN, Gottdiener JS, Scott CG, Enriquez-Sarano M. Burden of valvular heart diseases: a population-based study. *Lancet*. 2006;368:1005–1011. doi: 10.1016/S0140-6736(06)69208-8

2. Basso C, Perazzolo Marra M, Rizzo S, De Lazzari M, Giorgi B, Cipriani A, Frigo AC, Rigato I, Migliore F, Pilichou K, et al. Arrhythmic mitral valve prolapse and sudden cardiac death. *Circulation*. 2015;132:556–566. doi: 10.1161/CIRCULATIONAHA.115.016291

3. Levine RA, Hagége AA, Judge DP, Padala M, Dal-Bianco JP, Aikawa E, Beaudoin J, Bischoff J, Bouatia-Naji N, Bruneval P, et al. Mitral valve disease-morphology and mechanisms. *Nat Rev Cardiol*. 2015;12:689–710. doi: 10.1038/nrcardio.2015.161

4. Miller MA, Dukkipati SR, Turagam M, Liao SL, Adams DH, Reddy VY. Arrhythmic mitral valve prolapse: JACC review topic of the week. *J Am Coll Cardiol*. 2018;72:2904–2914. doi: 10.1016/j.jacc.2018.09.048

5. Borger MA, Mansour MC, Levine RA. Atrial fibrillation and mitral valve prolapse: time to intervene? *J Am Coll Cardiol*. 2019;73:275–277. doi: 10.1016/j.jacc.2018.11.018

6. Quintana E, Suri RM, Thalji NM, Daly RC, Dearani JA, Burkhart HM, Li Z, Enriquez-Sarano M, Schaff HV. Left ventricular dysfunction after mitral valve repair–the fallacy of "normal" preoperative myocardial function. *J Thorac Cardiovasc Surg*. 2014;148:2752–2760. doi: 10.1016/j.jtcvs.2014.07.029

7. Basso C, Iliceto S, Thiene G, Perazzolo MM. Mitral valve prolapse, ventricular arrhythmias, and sudden death. *Circulation*. 2019;140:952–964. doi: 10.1161/CIRCULATIONAHA.118.034075

8. Han H-C, Parsons SA, Curl CL, Teh AW, Raaijmakers AJA, Koshy AN, Leong T, Burrell LM, O'Donnell D, Vohra JK, et al. Systematic quantification of histologic ventricular fibrosis in isolated mitral valve prolapse and sudden cardiac death. *Heart Rhythm*. 2021;18:570–576. doi: 10.1016/j.hrthm.2020.12.021

9. Bui AH, Roujol S, Foppa M, Kissinger KV, Goddu B, Hauser TH, Zimetbaum PJ, Ngo LH, Manning WJ, Nezafat R, et al. Diffuse myocardial fibrosis in patients with mitral valve prolapse and ventricular arrhythmia. *Heart*. 2017;103:204–209. doi: 10.1136/heartjnl-2016-309303

10. Constant Dit Beaufils A-L, Huttin O, Jobbe-Duval A, Senage T, Filippetti L, Piriou N, Cueff C, Venner C, Mandry D, Sellal J-M, et al. Replacement myocardial fibrosis in patients with mitral valve prolapse: relation to mitral regurgitation, ventricular remodeling and arrhythmia. *Circulation*. 2021;143:1763–1774. doi: 10.1161/CIRCULATIONAHA.120.050214

11. Kitkungvan D, Nabi F, Kim RJ, Bonow RO, Khan MA, Xu J, Little SH, Quinones MA, Lawrie GM, Zoghbi WA, et al. Myocardial fibrosis in patients with primary mitral regurgitation with and without prolapse. *J Am Coll Cardiol*. 2018;72:823–834. doi: 10.1016/j.jacc.2018.06.048

12. Dejgaard LA, Skjølsvik ET, Lie ØH, Ribe M, Stokke MK, Hegbom F, Scheirlynck ES, Gjertsen E, Andresen K, Helle-Valle TM, et al. The mitral annulus disjunction arrhythmic syndrome. *J Am Coll Cardiol*. 2018;72:1600–1609. doi: 10.1016/j.jacc.2018.07.070

13. Toomer KA, Yu M, Fulmer D, Guo L, Moore KS, Moore R, Drayton KD, Glover J, Peterson N, Ramos-Ortiz S, et al. Primary cilia defects causing mitral valve prolapse. *Sci Transl Med*. 2019;11:eaax0290. doi: 10.1126/scitranslmed.aax0290

14. Yu M, Georges A, Tucker NR, Kyryachenko S, Toomer K, Schott JJ, Delling FN, Fernandez-Friera L, Solis J, Ellinor PT, et al. Genome-wide association study-driven gene-set analyses, genetic, and functional follow-up suggest GLIS1 as a susceptibility gene for mitral valve prolapse. *Circ Genom Precis Med*. 2019;12:e002497. doi: 10.1161/CIRCGEN.119.002497

15. Baumgartner H, Falk V, Bax JJ, De Bonis M, Hamm C, Holm PJ, Iung B, Lancellotti P, Lansac E, Rodriguez Muñoz D, et al. 2017 ESC/EACTS guidelines for the management of valvular heart disease. *Eur Heart J*. 2017;38:2739–2791. doi: 10.1093/eurheartj/ehx391

16. Durst R, Sauls K, Peal DS, deVlaming A, Toomer K, Leyne M, Salani M, Talkowski ME, Brand H, Perrocheau M, et al. Mutations in DCHS1 cause mitral valve prolapse. *Nature*. 2015;525:109–113. doi: 10.1038/nature14670

17. Fulmer D, Toomer K, Guo L, Moore K, Glover J, Moore R, Stairley R, Lobo G, Zuo X, Dang Y, et al. Defects in the exocyst-cilia machinery cause bicuspid aortic valve disease and aortic stenosis. *Circulation*. 2019;140:1331–1341. doi: 10.1161/CIRCULATIONAHA.119.038376

18. Sauls K, Toomer K, Williams K, Johnson AJ, Markwald RR, Hajdu Z, Norris RA. Increased infiltration of extra-cardiac cells in myxomatous valve disease. *J Cardiovasc Dev Dis*. 2015;2:200–213. doi: 10.3390/jcdd2030200

19. Toomer K, Sauls K, Fulmer D, Guo L, Moore K, Glover J, Stairley R, Bischoff J, Levine RA, Norris RA. Filamin-a as a balance between Erk/Smad activities during cardiac valve development. *Anat Rec (Hoboken)*. 2019;302:117–124. doi: 10.1002/ar.23911

20. Toomer KA, Fulmer D, Guo L, Drohan A, Peterson N, Swanson P, Brooks B, Mukherjee R, Body S, Lipschutz JH, et al. A role for primary cilia in aortic valve development and disease. *Dev Dyn*. 2017;246:625–634. doi: 10.1002/dvdy.24524

21. Rogers JD, Richardson WJ. Fibroblast mechanotransduction network predicts targets for mechano-adaptive infarct therapies. *BioRxiv*. August 14, 2020. doi: 10.1101/2020.08.13.250001

22. Zeigler AC, Richardson WJ, Holmes JW, Saucerman JJ. A computational model of cardiac fibroblast signaling predicts context-dependent drivers of myofibroblast differentiation. *J Mol Cell Cardiol*. 2016;94:72–81. doi: 10.1016/j.yjmcc.2016.03.008

23. van Putten S, Shafieyan Y, Hinz B. Mechanical control of cardiac myofibroblasts. *J Mol Cell Cardiol*. 2016;93:133–142. doi: 10.1016/j.yjmcc.2015.11.025

24. Milan M, Pace V, Maiullari F, Chirivì M, Baci D, Maiullari S, Madaro L, Maccari S, Stati T, Marano G, et al. Givinostat reduces adverse cardiac remodeling through regulating fibroblasts activation. *Cell Death Dis*. 2018;9:108. doi: 10.1038/s41419-017-0174-5

25. Schafer S, Viswanathan S, Widjaja AA, Lim W-W, Moreno-Moral A, DeLaughter DM, Ng B, Patone G, Chow K, Khin E, et al. IL-11 is a crucial determinant of cardiovascular fibrosis. *Nature*. 2017;552:110–115. doi: 10.1038/nature24676

26. Travers JG, Kamal FA, Robbins J, Yutzey KE, Blaxall BC. Cardiac fibrosis: the fibroblast awakens. *Circ Res*. 2016;118:1021–1040. doi: 10.1161/CIRCRESAHA.115.306565

27. Weber KT. Cardiac interstitium in health and disease: the fibrillar collagen network. *J Am Coll Cardiol*. 1989;13:1637–1652. doi: 10.1016/0735-1097(89)90360-4

28. Dina C, Bouatia-Naji N, Tucker N, Delling FN, Toomer K, Durst R, Perrocheau M, Fernandez-Friera L, Solis J, Le Tourneau T, et al. Genetic

association analyses highlight biological pathways underlying mitral valve prolapse. *Nat Genet*. 2015;47:1206–1211. doi: 10.1038/ng.3383

29. Villalobos E, Criollo A, Schiattarella GG, Altamirano F, French KM, May HI, Jiang N, Nguyen NUN, Romero D, Roa JC, et al. Fibroblast primary cilia are required for cardiac fibrosis. *Circulation*. 2019;139:2342–2357. doi: 10.1161/CIRCULATIONAHA.117.028752

30. Gerdes JM, Katsanis N. Ciliary function and Wnt signal modulation. *Curr Top Dev Biol*. 2008;85:175–195. doi: 10.1016/S0070-2153(08)00807-7

31. Fulmer D, Toomer KA, Glover J, Guo L, Moore K, Moore R, Stairley R, Gensemer C, Abrol S, Rumph MK, et al. Desert hedgehog-primary cilia cross talk shapes mitral valve tissue by organizing smooth muscle actin. *Dev Biol*. 2020;463:26–38. doi: 10.1016/j.ydbio.2020.03.003

32. Rohatgi R, Milenkovic L, Scott MP. Patched1 regulates hedgehog signaling at the primary cilium. *Science*. 2007;317:372–376. doi: 10.1126/science.1139740

33. Arrighi N, Lypovetska K, Moratal C, Giorgetti-Peraldi S, Dechesne CA, Dani C, Peraldi P. The primary cilium is necessary for the differentiation and the maintenance of human adipose progenitors into myofibroblasts. *Sci Rep*. 2017;7:15248. doi: 10.1038/s41598-017-15649-2

34. Clement CA, Ajbro KD, Koefoed K, Vestergaard ML, Veland IR, Henriques de Jesus MP, Pedersen LB, Benmerah A, Andersen CY, Larsen LA, et al. TGF-beta signaling is associated with endocytosis at the pocket region of the primary cilium. *Cell Rep*. 2013;3:1806–1814. doi: 10.1016/j.celrep.2013.05.020

35. Labour MN, Riffault M, Christensen ST, Hoey DA. TGFbeta1—induced recruitment of human bone mesenchymal stem cells is mediated by the primary cilium in a SMAD3-dependent manner. *Sci Rep*. 2016;6:35542. doi: 10.1038/srep35542

36. Jones TJ, Adapala RK, Geldenhuys WJ, Bursley C, AbouAlaiwi WA, Nauli SM, Thodeti CK. Primary cilia regulates the directional migration and barrier integrity of endothelial cells through the modulation of hsp27 dependent actin cytoskeletal organization. *J Cell Physiol*. 2012;227:70–76. doi: 10.1002/jcp.22704

37. Song B, Haycraft CJ, Seo HS, Yoder BK, Serra R. Development of the post-natal growth plate requires intraflagellar transport proteins. *Dev Biol*. 2007;305:202–216. doi: 10.1016/j.ydbio.2007.02.003

38. Wang Z, Wann AK, Thompson CL, Hassen A, Wang W, Knight MM. IFT88 influences chondrocyte actin organization and biomechanics. *Osteoarthritis Cartilage*. 2016;24:544–554. doi: 10.1016/j.joca.2015.10.003

39. Calder BW, Matthew Rhett J, Bainbridge H, Fann SA, Gourdie RG, Yost MJ. Inhibition of connexin 43 hemichannel-mediated ATP release attenuates early inflammation during the foreign body response. *Tissue Eng Part A*. 2015;21:1752–1762. doi: 10.1089/ten.tea.2014.0651

40. Heidt T, Courties G, Dutta P, Sager HB, Sebas M, Iwamoto Y, Sun Y, Da Silva N, Panizzi P, van der Laan AM, et al. Differential contribution of monocytes to heart macrophages in steady-state and after myocardial infarction. *Circ Res*. 2014;115:284–295. doi: 10.1161/CIRCRESAHA.115.303567

41. Hulsmans M, Clauss S, Xiao L, Aguirre AD, King KR, Hanley A, Hucker WJ, Wülfers EM, Seemann G, Courties G, et al. Macrophages facilitate electrical conduction in the heart. *Cell*. 2017;169:510–522.e520. doi: 10.1016/j.cell.2017.03.050

42. Ishikawa H, Marshall WF. Ciliogenesis: building the cell's antenna. *Nat Rev Mol Cell Biol*. 2011;12:222–234. doi: 10.1038/nrm3085

43. Ishikawa H, Marshall WF. Mechanobiology of ciliogenesis. *Bioscience*. 2014;64:1084–1091. doi: 10.1093/biosci/biu173

44. Kawasaki M, Ezura Y, Hayata T, Notomi T, Izu Y, Noda M. TGF-beta suppresses Ift88 expression in chondrocytic ATDC5 cells. *J Cell Physiol*. 2015;230:2788–2795. doi: 10.1002/jcp.25005

45. Seeger-Nukpezah T, Golemis EA. The extracellular matrix and ciliary signaling. *Curr Opin Cell Biol*. 2012;24:652–661. doi: 10.1016/j.ceb.2012.06.002

46. Mangos S, Lam PY, Zhao A, Liu Y, Mudumana S, Vasilyev A, Liu A, Drummond IA. The ADPKD genes pkd1a/b and pkd2 regulate extracellular matrix formation. *Dis Model Mech*. 2010;3:354–365. doi: 10.1242/dmm.003194

47. Kawasaki M, Nariswari NA, Berg NWEVD, Neefs J, Meulendijks ER, Wesselink R, Baalman SWE, Boven WJPV, Driessen AHG, De Groot JR. The primary cilium, a sensory apparatus of cells regulates the profibrotic capacity of fibroblasts in atrial fibrillation. *Eur Heart J*. 2019;40:2111. doi: 10.1093/eurheartj/ehz745.0365

48. Gourdie RG, Dimmeler S, Kohl P. Novel therapeutic strategies targeting fibroblasts and fibrosis in heart disease. *Nat Rev Drug Discov*. 2016;15:620–638. doi: 10.1038/nrd.2016.89

49. Jiang J, Hoagland D, Palatinus JA, He H, Iyyathurai J, Jourdan LJ, Bultynck G, Wang Z, Zhang Z, Schey K, et al. Interaction of alpha carboxyl terminus 1 peptide with the connexin 43 carboxyl terminus preserves left ventricular function after ischemia-reperfusion injury. *J Am Heart Assoc*. 2019;8:e012385. doi: 10.1161/JAHA.119.012385

50. Stout CE, Costantin JL, Naus CC, Charles AC. Intercellular calcium signaling in astrocytes via ATP release through connexin hemichannels. *J Biol Chem*. 2002;277:10482–10488. doi: 10.1074/jbc.M109902200

51. Lu D, Soleymani S, Madakshire R, Insel PA. ATP released from cardiac fibroblasts via connexin hemichannels activates profibrotic P2Y2 receptors. *FASEB J*. 2012;26:2580–2591. doi: 10.1096/fj.12-204677

52. Dosch M, Zindel J, Jebbawi F, Melin N, Sanchez-Taltavull D, Stroka D, Candinas D, Beldi G. Connexin-43-dependent ATP release mediates macrophage activation during sepsis. *eLife*. 2019;8:e42670. doi: 10.7554/eLife.42670

53. Kim JC, Perez-Hernandez M, Alvarado FJ, Maurya SR, Montnach J, Yin Y, Zhang M, Lin X, Vasquez C, Heguy A, et al. Disruption of Ca(2+)i homeostasis and connexin 43 hemichannel function in the right ventricle precedes overt arrhythmogenic cardiomyopathy in plakophilin-2-deficient mice. *Circulation*. 2019;140:1015–1030. doi: 10.1161/CIRCULATIONAHA.119.039710

54. Nouet J, Himelman E, Lahey KC, Zhao Q, Fraidenraich D. Connexin-43 reduction prevents muscle defects in a mouse model of manifesting Duchenne muscular dystrophy female carriers. *Sci Rep*. 2020;10:5683. doi: 10.1038/s41598-020-62844-9

55. Zhang J, Chandrasekaran G, Li W, Kim D-Y, Jeong IY, Lee S-H, Liang T, Bae JY, Choi I, Kang H, et al. Wnt-PLC-IP3-connexin-Ca(2+) axis maintains ependymal motile cilia in zebrafish spinal cord. *Nat Commun*. 2020;11:1860. doi: 10.1038/s41467-020-15248-2

56. Ermakov S, Gulhar R, Lim L, Bibby D, Fang Q, Nah G, Abraham TP, Schiller NB, Delling FN. Left ventricular mechanical dispersion predicts arrhythmic risk in mitral valve prolapse. *Heart*. 2019;105:1063–1069. doi: 10.1136/heartjnl-2018-314269

57. David TE, David CM, Tsang W, Lafreniere-Roula M, Manlhiot C. Long-term results of mitral valve repair for regurgitation due to leaflet prolapse. *J Am Coll Cardiol*. 2019;74:1044–1053. doi: 10.1016/j.jacc.2019.06.052

58. Grinberg D, Cottinet PJ, Thivolet S, Audigier D, Capsal JF, Le MQ, Obadia JF. Measuring chordae tension during transapical neochordae implantation: toward understanding objective consequences of mitral valve repair. *J Thorac Cardiovasc Surg*. 2019;158:746–755. doi: 10.1016/j.jtcvs.2018.10.029

59. Grinberg D, Le MQ, Kwon YJ, Fernandez MA, Audigier D, Ganet F, Capsal JF, Obadia JF, Cottinet PJ. Mitral valve repair based on intraoperative objective measurement. *Sci Rep*. 2019;9:4677. doi: 10.1038/s41598-019-41173-6

60. Paulsen MJ, Imbrie-Moore AM, Wang H, Bae JH, Hironaka CE, Farry JM, Lucian HJ, Thakore AD, MacArthur JW, Cutkosky MR, et al. Mitral chordae tendineae force profile characterization using a posterior ventricular anchoring neochordal repair model for mitral regurgitation in a three-dimensional-printed ex vivo left heart simulator. *Eur J Cardiothorac Surg*. 2020;57:535–544. doi: 10.1093/ejcts/ezz258

61. Imbrie-Moore AM, Paulsen MJ, Zhu Y, Wang H, Lucian HJ, Farry JM, MacArthur JW, Ma M, Woo YJ. A novel cross-species model of Barlow's disease to biomechanically analyze repair techniques in an ex vivo left heart simulator. *J Thorac Cardiovasc Surg*. 2021;161:1776–1783. doi: 10.1016/j.jtcvs.2020.01.086

SUPPLEMENTAL MATERIAL

Table 1. Pre-operative baseline characteristics.

Variable	Patients (n=6)
Clinical data	
Age, years	59.6 ± 5.7
Age ≥ 70, n (%)	0 (0)
BMI	24.2 ± 1.0
Male, n (%)	6 (100)
Atrial fibrilation, n (%)	1 (16.7)
Hypertension, n (%)	3 (50.0)
Diabetes, n (%)	0 (0.0)
Coronary artery disease, n (%)	0 (0)
NYHA functional class III-IV	2 (33.3)
Echocardiographic data	
LVEF (%)	59.3 ± 4.6
LVEDD (mm)	61.8 ± 4.3
LVESD (mm)	43.3 ± 3.2
PISA radius (cm)	1.2 ± 0.2
EROA (cm²)	0.5 ± 0.1
Regurgitant volume (ml)	69.3 ± 7.3
Regurgitant fraction (%)	59.5 ± 9.6
Vena contracta MR (mm)	7.2 ± 2.4
MR Grade 4+, n (%)	6 (100)
sPAP (mmHg)	44.7 ± 17.4

NYHA: New York Heart Association; LVEF: left ventricular ejection fraction; LVEDD: left ventricular end diastolic diameter; LVESD: left ventricular end systolic diameter; PISA: proximal isovelocity surface area; EROA: effective regurgitant orifice area; MR, mitral regurgitation; sPAP: systolic pulmonary artery pressure.

Tables S2, S3: Inputs for computational modeling parameters.

Species information

module	ID	name	Yinit	Ymax	tau	type	gene name	notes
g-coupled	AngII	angiotensin II	0	1	1	protein	AGT	
g-coupled	AT1R	angiotensin II receptor type 1	0	1	0.1	protein	AGTR1;AGTR2	
g-coupled	AGT	angiotensinogen	0	1	10	protein	AGT	
g-coupled	ACE	angiotensin converting enzyme	0	1	0.1	protein	ACE; ACE2	
g-coupled	NOX	NAD(P)H oxidase	0	1	0.1	protein	NOX4; NOX5	
g-coupled	ROS	reactive oxygen species	0	1	0.1	protein		
g-coupled	ET1	endothelin 1	0	1	1	protein	EDN1	
g-coupled	ETAR	endothelin 1 receptor A	0	1	0.1	protein	EDNRA	
g-coupled	DAG	diacyl-glycerol	0	1	0.1	small		
g-coupled	PKC	protein kinase C	0	1	0.1	protein	PRKCA; PRKCE;	
pressure/stretch	TRPC	transient receptor potential canonical	0	1	0.1	protein	TRPC6;TRPC3	
g-coupled	NE	norepinephrine	0	1	1	small		
g-coupled	BAR	beta adrenergic receptor 1 or 2	0	1	0.1	protein	ADRB1; ADRB2	
g-coupled	Forskolin		0	1	1	small		
g-coupled	AC	adenylate cyclase	0	1	0.1	protein	ADCY6	
g-coupled	cAMP	cyclic adenosine monophosphate	0	1	0.1	small		
g-coupled	PKA	protein kinase A	0	1	0.1	protein	PRKACA	
g-coupled	CREB	cAMP response-element binding protein	0	1	0.1	protein	CREB1; CREB3	
g-coupled	CBP	CREB - binding protein	0	1	0.1	protein	CREBBP	
growth factor	TGFB	transforming growth factor beta 1	0	1	1	protein	TGFB1	
growth factor	TGFB1R	TGFB receptor	0	1	0.1	protein	TGFBR1; TGFBR2	
growth factor	smad3	small mothers against decapentaplegic 2 and 3	0	1	0.1	protein	SMAD2; SMAD3	
growth factor	smad7		0	1	10	protein	SMAD7	
growth factor	latentTGFB	TGFB1 with latent protein complex	0	1	10	protein	TGFB1	
growth factor	BAMBI	BMP and activin bound inhibitor	0	1	0.1	protein	BAMBI	
growth factor	PDGF	platelet derived growth factor	0	1	1	protein	PDGFA; PDGFB; PDGFD	
growth factor	PDGFR	platelet derived growth factor receptor	0	1	0.1	protein	PDGFRA; PDGFRB	
g-coupled	NP	natriuretic peptide	0	1	1	protein	NPPA; NPPB	
g-coupled	NPRA	natriuretic peptide receptor	0	1	0.1	protein	NPR1; NPR2; NPR3	
g-coupled	cGMP	cyclic guanosine monophosphate	0	1	0.1	small		
g-coupled	PKG	protein kinase G	0	1	0.1	protein	PRKG1	
pressure/stretch	tension	stretch	0	1	1	process		
pressure/stretch	B1int	beta 1 integrin	0	1	0.1	protein	ITGB1	
pressure/stretch	Rho	a Rho-dependent GTPase	0	1	0.1	protein	RHOA	
pressure/stretch	ROCK	rho associated protein kinase	0	1	0.1	protein	ROCK1	
pressure/stretch	Ca	calcium	0	1	0.1	small		
pressure/stretch	calcineurin	calcineurin	0	1	0.1	protein	PPP3CA; PPP3CB	
pressure/stretch	NFAT	nuclear factor of activated T-cells	0	1	0.1	protein	NFATC1	
cytokine	IL6	interleukin-6	0	1	1	protein	IL6	
cytokine	gp130	IL-6 receptor complexed to gp130 for signal transc	0	1	0.1	protein	IL6ST; IL6R	
cytokine	STAT	signal transducers and activators of transcription 1	0	1	0.1	protein	STAT1; STAT3	
cytokine	IL1	interleukin-1 alpha and beta	0	1	1	protein	IL1B; IL1A	
cytokine	IL1RI	IL1 receptor type I	0	1	0.1	protein	IL1R1	
cytokine	TNFa	tissue necrosis factor alpha	0	1	1	protein	TNF	
cytokine	TNFaR	TNF alpha receptor	0	1	0.1	protein	TNFRSF1A;TNFRSF1B	
cytokine	NFKB	nuclear factor kappa-light-chain-enhancer of activa	0	1	0.1	protein	NFKB1	
cytokine	PI3K	phosphoinositide 3-kinase	0	1	0.1	protein	PIK3CA	
cytokine	Akt	protein kinase B	0	1	0.1	protein	AKT1; AKT2; AKT3	
MAPK	p38	a MAP kinase	0	1	0.1	protein	MAPK14	
MAPK	TRAF	tnf receptor associated factor either 2/6	0	1	0.1	protein	TRAF6	
MAPK	ASK1	apoptosis signal related kinase 1	0	1	0.1	protein	MAP3K5	
MAPK	MKK3	mitogen activated protein kinase kinase	0	1	0.1	protein	MAP2K3	
MAPK	PP1	protein phosphatase 1	0	1	0.1	protein	PPP1CA; PPP1CB; PPP1CC	
MAPK	JNK	a MAP kinase	0	1	0.1	protein	MAPK8	
MAPK	abl	abl tyrosine kinase	0	1	0.1	protein	ABL1; ABL2	
MAPK	Rac1	a Rho-dependent GTPase	0	1	0.1	protein	RAC1	
MAPK	MEKK1	a MAP3K associated with p38 and JNK	0	1	0.1	protein	MAP3K1	
MAPK	MKK4	a MAP2K associated with p38 and JNK	0	1	0.1	protein	MAP2K4	
MAPK	ERK	a MAP kinase	0	1	0.1	protein	MAPK1; MAPK3	
MAPK	Ras	representing the family of GTPases	0	1	0.1	protein	KRAS	
MAPK	Raf	family of raf protein serine/threonine kinases	0	1	0.1	protein	RAF1	
MAPK	MEK1	a MAP2K mainly specific to ERK	0	1	0.1	protein	MAP2K1	
adhesion	FAK	focal adhesion kinase	0	1	0.1	protein	PTK2	
g-coupled	epac	exchange protein activated by cAMP 1	0	1	0.1	protein	RAPGEF3	
adhesion	Factin	polymerized actin	0	1	1	protein	ACTG1	
adhesion	FA	stabilization of focal adhesions	0	1	1	complex		
growth	cmyc	myc transcription factor	0	1	0.1	protein	MYC	
growth	CTGF	connective tissue growth factor	0	1	0.1	protein	CTGF	
growth	proliferation	proliferation	0	1	10	event		
adhesion	SRF	serum response factor	0	1	0.1	protein	SRF	
ECM	EDAFN	extra domain A of fibronectin	0	1	10	protein	FN1	
adhesion	aSMA	alpha-smooth muscle actin	0	1	10	protein	ACTA2	
MAPK	AP1	activator protein 1	0	1	0.1	protein	JUN; FOS	
ECM	TIMP1	tissue inhibitor of metalloproteinase 1	0	1	10	protein	TIMP1	
ECM	TIMP2	tissue inhibitor of metalloproteinase 2	0	1	10	protein	TIMP2	
ECM	PAI1	plasminogen activator inhibitor 1	0	1	10	protein	SERPINE1	

Category	Short name	Description				Type	Gene
ECM	proMMP14	inactive MMP14	0	1	10	protein	MMP14
ECM	proMMP1	inactive MMP1	0	1	10	protein	MMP1
ECM	proMMP2	inactive MMP2	0	1	10	protein	MMP2
ECM	proMMP9	inactive MMP9	0	1	10	protein	MMP9
ECM	fibronectin	fibronectin	0	1	10	protein	FN1
ECM	periostin	periostin	0	1	10	protein	POSTN
ECM	proCI	procollagen I	0	1	10	protein	COL1A1
ECM	proCIII	procollagen III	0	1	10	protein	COL3A1
pressure/stretch	B3int	beta 3 integrin	0	1	0.1	protein	ITGB3
adhesion	Src	proto-oncogene tyrosine-protein kinase Src	0	1	0.1	protein	SRC1
MAPK	Grb2	growth factor receptor-bound protein 2	0	1	0.1	protein	GRB2
adhesion	p130Cas	breast cancer anti-estrogen resistance protein 1	0	1	0.1	protein	BCAR1
pressure/stretch	YAP	yes-associated protein 1	0	1	0.1	protein	YAP1
adhesion	MRTF	myocardin-related transcription factor A	0	1	0.1	protein	MRTFA; MKL1
adhesion	Gactin	monomeric actin	0	1	1	protein	ACTG1
ECM	TNC	tenascin-c	0	1	10	protein	TNC
growth	mTORC1	mammalian target of rapamyocin complex 1	0	1	0.1	complex	
growth	mTORC2	mammalian target of rapamyocin complex 2	0	1	0.1	complex	
growth	p70S6K	p70-S6 kinase 1	0	1	0.1	protein	RPS6KB1
growth	EBP1	eukaryotic translation initiation factor 4E-binding	0	1	0.1	protein	EIF4EBP1
pressure/stretch	syndecan4	syndecan 4	0	1	0.1	protein	SDC4
ECM	proMMP3	inactive MMP3	0	1	1	protein	MMP3
ECM	proMMP8	inactive MMP8	0	1	1	protein	MMP8
ECM	proMMP12	inactive MMP12	0	1	1	protein	MMP12
ECM	thrombospondin4	thrombospondin 4	0	1	10	protein	THBS4
ECM	osteopontin	osteopontin	0	1	10	protein	SPP1
adhesion	contractility	intracellular tension	0	1	10	event	
pressure/stretch	RhoGEF	a Rho guanine nucleotide exchange factor	0	1	0.1	protein	
pressure/stretch	RhoGDI	a Rho GDP-dissociation inhibitor	0	1	0.1	protein	
adhesion	talin	talin 1	0	1	0.1	protein	TLN1
adhesion	vinculin	vinculin	0	1	0.1	protein	VCL
adhesion	paxillin	paxillin	0	1	0.1	protein	PXN
adhesion	MLC	myosin regulatory light chain	0	1	0.1	protein	MYL2
Cilia	Cilia	primary cilia	0	1	1	complex	
Cilia	PKD1	polycystin-1	0	1	1	protein	
Cilia	PKD2	polycystin-2	0	1	1	protein	
pressure/stretch	TRPV4	TRPV channel	0	1	1	protein	
g-coupled	IP3R	inositol triphosphate receptor	0	1	1	protein	
Cilia	DZIP1	DAZ Interacting Zinc Finger Protein 1	0	1	1	protein	
Cilia	CBY1	Protein chibby homolog 1	0	1	1	protein	
cytokine	Bcatenin	Beta-catenin	0	1	1	protein	
g-coupled	SMO	Smoothened	0	1	1	protein	
cytokine	DHH	Deseart Hedgehog	0	1	1	protein	
cytokine	TIAM1	T-lymphoma invasion and metastasis-inducing pro	0	1	1	protein	
cytokine	WNT	WNT	0	1	1	protein	
cytokine	Pak1	p21 (Rac1) Activated Kinase 1	0	1	1	protein	
cytokine	Flna	filamin-a	0	1	1	protein	
cytokine	Hic5	Transforming Growth Factor Beta 1 Induced Tra	0	1	1	protein	
cytokine	Ptch1	Patched 1	0	1	1	protein	
cytokine	Gli2	GLI Family Zinc Finger 2	0	1	1	protein	
cytokine	Runx2	HH pathway transcription factor	0	1	1	protein	
ECM	ADAMTS4	A Disintegrin and Metalloproteinase with Thromb	0	1	10	protein	
ECM	ADAMTS5	A Disintegrin and Metalloproteinase with Thromb	0	1	10	protein	
ECM	ADAMTS9	A Disintegrin and Metalloproteinase with Thromb	0	1	10	protein	
ECM	proMMP13	inactive MMP13	0	1	10	protein	
cytokine	Fz	Frazzled	0	1	1	protein	
cytokine	Dvl	Disheveled	0	1	1	protein	
cytokine	Groucho	Groucho	0	1	1	protein	
cytokine	TCF	TCF/LEF1 transcription factors	0	1	1	protein	
ECM	versican	Versican	0	1	1	protein	
protein	GSK3B	GSK3B	0	1	1	protein	

Reaction Information

module	ID	Rule	Weight	n	EC50	source	notes	PMID	Secondary Reference	Tertiary Reference	AND references
input	i1	=> AngII	0.1	1.3	0.55	neonatal rat cardiac fibroblasts	increased via RAS in hypertension and heart failure	10362677			
input	i2	=> TGFB	0.1	1.3	0.55		increased in response to injury	20538689			
input	i3	=> tension	0.1	1.3	0.55		increased with integrin stimulation	9547793			
input	i4	=> IL6	0.1	1.3	0.55		increased in hypertension	19234091			
input	i5	=> IL1	0.1	1.3	0.55			19631653			
input	i6	=> TNFa	0.1	1.3	0.55			10591022			
input	i7	=> NE	0.1	1.3	0.55		most likely NE signaling	3948363			
input	i8	=> PDGF	0.1	1.3	0.55		increased post-MI	20538689			
input	i9	=> ET1	0.1	1.3	0.55		increased from stretch of vascular endothelial cells	12695528			
input	i10	=> NP	0.1	1.3	0.55		increased in pressure	17991884			
input	i11	=> Forskolin	0	1.3	0.55						
fback	r1	proMMP9 & latentTGFB => TGFB	0.25	1.3	0.55	in vitro	release of latent protein	10652271	MC3T3-E1 12226090		
fback	r2	proMMP2 & latentTGFB => TGFB	0.25	1.3	0.55	in vitro	release of latent protein	10652271	MC3T3-E1 12226090		
fback	r3	ACE & AGT => AngII	0.25	1.3	0.55	neonatal cardiac fibroblasts	enzymatic modification	10790312	in vitro 13295487		
fback	r4	CREB + CBP => IL6	0.25	1.3	0.55	neonatal rat cardiac fibroblasts	txn	11597988	mouse cardiac fibroblasts 16466739	10405202	
fback	r5	NFKB => IL6	0.25	1.3	0.55	neonatal rat cardiac fibroblasts	txn	11597988	16466739		
fback	r6	AP1 => IL6	0.25	1.3	0.55	neonatal rat cardiac fibroblasts	txn	11597988	sv40 murine cells 16466739		
fback	r7	AP1 => ET1	0.25	1.3	0.55	neonatal rat cardiac fibroblasts	txn	12695528	bovine aortic endothelial cells 1918021		
middle	r8	AngII => AT1R	1	1.3	0.55	neonatal rat cardiac fibroblasts	receptor binding	8348686	adult rat cardiac fibroblasts 16024575		
middle	r9	AT1R => NOX	1	1.3	0.55	adult rat cardiac fibroblast	-	15106793	neonatal rat cardiac fibroblasts 11597988		
middle	r10	NOX => ROS	1	1.3	0.55	adult rat cardiac fibroblast	enzymatic production	15106793	adult rat cardiac fibroblasts 16531806		
middle	r11	IL6 => gp130	1	1.3	0.55	neonatal rat cardiac fibroblasts	receptor binding	19234091	COS7 cells 1602143		
middle	r12	ROS => ERK	1	1.3	0.55	neonatal rat cardiac fibroblasts	activation	11597988	neonatal rat cardiac fibroblasts 14642698	12695528	
middle	r13	ROS => p38	1	1.3	0.55	neonatal rat cardiac fibroblasts	activation	11597988	neonatal rat cardiac fibroblasts 24882408	12695528	
middle	r14	ROS => JNK	1	1.3	0.55	neonatal rat cardiac fibroblasts	activation	11597988	neonatal rat cardiac fibroblasts 12695528		
middle	r15	IL1RI => NFKB	1	1.3	0.55	neonatal rat cardiac fibroblasts	release of blocking and increased abundance	11597988	human foreskin fibroblasts 1906501		
middle	r16	gp130 => STAT	1	1.3	0.55	neonatal mouse fibroblasts	activation (via JAK)	19234091	murine proB cell line 9874564		
middle	r17	TNFaR => PI3K	1	1.3	0.55	human cardiac fibroblast	activation	17560598	human cardiac fibroblast 17612514		
middle	r18	!AT1R & !JNK & p38 => AGT	1	1.3	0.55	human cardiac fibroblasts	txn	18926830	neonatal rat cardiac fibroblasts 21131638		11192370
middle	r19	TGFB1R & !PKG & !smad7 => smad3	1	1.3	0.55	adult rat cardiac fibroblast	activation	17513491	COS7 cells 9335507, 9215638	17991884, 17038494	
output	r20	smad3 & CBP & ERK => CTGF	1	1.3	0.55	adult rat cardiac fibroblasts	txn	18586263	mouse cardiac fibroblasts 22749815	11013125	12368229, 16959941
output	r21	STAT => proMMP2	1	1.3	0.55	neonatal rat cardiac fibroblasts	txn	15350851	human lung cell lines 24573038		
output	r22	STAT => proMMP9	1	1.3	0.55	mouse cardiac fibroblasts	txn	19234091	human genome database 18258475		
output	r23	smad3 & CBP => periostin	1	1.3	0.55	adult rat cardiac fibroblasts	txn	21367774	gingival fibroblasts 24004653		16959941
output	r24	CREB & CBP => periostin	1	1.3	0.55	adult rat cardiac fibroblasts	txn	21367774	murine dermal fibroblast 24577408		16959941
middle	r25	ERK => NFKB	1	1.3	0.55	human cardiac fibroblast	activation	17921324	periodontal ligament fibroblast 21757573		
middle	r26	p38 => NFKB	1	1.3	0.55	human cardiac fibroblast	activation	17921324	NIH-3T3 (via CBP) 11259436		
output	r27	NFKB & AP1 & !smad3 => proMMP1	1	1.3	0.55	human cardiac fibroblast	txn	17921324	human dermal fibroblasts 11502752	12525489	
middle	r28	ETAR => ROS	1	1.3	0.55	neonatal rat cardiac fibroblasts	activation	12695528	neonatal rat cardiac fibroblasts 16391241		
middle	r29	ERK => AP1	1	1.3	0.55	neonatal rat cardiac fibroblasts	activation	12695528	human lung fibroblast 10862759		
output	r30	AP1 => proMMP2	1	1.3	0.55	human cardiac fibroblasts	txn	17921324	neonatal rat cardiac fibroblasts 12371906		
output	r31	AP1 & NFKB => proMMP9	1	1.3	0.55	human cardiac fibroblasts	txn	17560598	human foreskin fibroblasts 9755853		
output	r32	AP1 => TIMP1	1	1.3	0.55	human cardiac fibroblasts	txn	17921324	human foreskin fibroblasts 9182725		
output	r33	AP1 => TIMP2	1	1.3	0.55	human cardiac fibroblasts	txn	17921324	3T3 and rat fibroblast 8112602		
middle	r34	PKC & tension => B1int	1	1.3	0.55	adult rat cardiac fibroblasts	activation	15949469	mouse embryonic fibroblasts 12110574	21131638	
middle	r35	cAMP => PKA	1	1.3	0.55	adult rat cardiac fibroblasts	activation	11054474	cardiac fibroblast 21977288		
output	r36	smad3 & CBP => fibronectin	1	1.3	0.55	human lung fibroblast	txn	16707625	human cardiac fibroblast 11013125		
middle	r37	!smad3 => CBP	1	1.3	0.55	adult rat cardiac fibroblasts	depletion of txn factor binding partner	16959941	human dermal fibroblasts 10918613		
middle	r38	!CREB => CBP	1	1.3	0.55	adult rat cardiac fibroblasts	depletion of txn factor binding partner	16959941	3T3 cells 8028671		
middle	r39	tension => B1int	1	1.3	0.55	neonatal rat cardiac fibroblasts	activation	21131638	NIH-3T3 15760908		
output	r40	NFAT => EDAFN	1	1.3	0.55	neonatal mice cardiac fibroblast	txn activation	23178899	rat cardiac fibroblasts 23142541		
middle	r41	TGFB1R => ACE	1	1.3	0.55	rat cardiac fibroblasts	increased txn	11967821	human cardiac myofibroblasts 18223028		
middle	r42	TGFB & !BAMBI => TGFB1R	1	1.3	0.55	mice cardiac fibroblast	binding to receptor	22960625	mouse cardiac fibroblasts 24078695		
middle	r43	AP1 => proliferation	1	1.3	0.55	adult rat cardiac fibroblasts	via activation of Kca3.1 channels	23500546	adult rat cardiac fibroblasts 17483238		
middle	r44	PKA => CREB	1	1.3	0.55	rat cardiac fibroblasts	activation	11054474	neonatal rat myofibroblasts 11909979		
middle	r45	CREB => proliferation	1	1.3	0.55	rat cardiac fibroblasts		11054474	rat cardiac fibroblasts 17483238		
middle	r46	NE => BAR	1	1.3	0.55	rat cardiac fibroblasts	receptor binding	11054474	rat pineal gland 7700241		
middle	r47	ET1 => ETAR	1	1.3	0.55	neonatal rat cardiac fibroblasts	receptor binding	12695528	adult rat cardiac fibroblasts 8313418		
middle	r48	CTGF => proliferation	1	1.3	0.55	human cardiac fibroblast		11013125	adult rat cardiac fibroblasts 17483238		
middle	r49	IL1 => IL1RI	1	1.3	0.55	mouse cell line	receptor binding	8327496	neonatal rat cardiac fibroblasts 7769098		
middle	r50	PKC => proliferation	1	1.3	0.55	adult rat cardiac fibroblasts	activation	10756114	adult rat cardiac fibroblasts 17483238		
output	r51	smad3 & CBP & !epac => proCI	1	1.3	0.55	adult rat cardiac fibroblasts	txn	17513491	adult rat cardiac fibroblasts 17513491	11279127 18434542, 23845590	
output	r52	smad3 & CBP & !epac => proCIII	1	1.3	0.55	adult rat cardiac fibroblasts	txn	17513491	adult rat cardiac fibroblasts 17513491	11279127 18434542, 23845590	
output	r53	AP1 => proMMP14	1	1.3	0.55	mouse cardiac fibroblasts	correlated increase with cFOS	22287584	mouse embryonic fibroblasts 17348021		
middle	r54	PDGF => PDGFR	1	1.3	0.55	adult rat cardiac fibroblasts	receptor binding	11230972	rat cardiac fibroblasts 24427322		
middle	r55	BAR => AC	1	1.3	0.55	adult rat cardiac fibroblasts	activation	12711600	rat cardiac fibroblasts 17934720		
middle	r56	BAR & AT1R => AC	1	1.3	0.55	adult rat cardiac fibroblasts	activation with potentiation	12711600	rat dermal fibroblasts 1330500		
middle	r57	AC => cAMP	1	1.3	0.55	adult rat cardiac fibroblasts	activation	12711600	human pulmonary fibroblast 15075208		
middle	r58	FAK =>MEKK1	1	1.3	0.55	mouse embryonic fibroblasts	activation	17409352	mouse embryonic fibroblasts 12458213	21131638	
output	r59	AP1 => latentTGFB	1	1.3	0.55	mouse lung fibroblasts	txn activation	20141610	adult rat cardiac fibroblasts 21367774 22429882, 19374881		
middle	r60	cAMP => epac	1	1.3	0.55	adult rat cardiac fibroblasts	activation	18434542	NIH-3T3 9853756		
middle	r61	Rho => ROCK	1	1.3	0.55	rat embryonic fibroblasts	activation	16043513	rat cardiac fibroblasts 17456553		
middle	r62	TNFa => TNFaR	1	1.3	0.55	human cardiac fibroblast	receptor binding	17560598	mouse cardiac fibroblasts 23337087		
middle	r63	NP => NPRA	1	1.3	0.55	adult rat cardiac fibroblast	receptor binding	16986166	COS7 cells 11595171		
middle	r64	NPRA => cGMP	1	1.3	0.55	adult rat cardiac fibroblast	activation	17991884	human cardiac fibroblast 16986166		
middle	r65	cGMP => PKG	1	1.3	0.55	adult rat cardiac fibroblast		17991884	mouse cardiac fibroblasts 21282499		
middle	r66	Ras => Raf	1	1.3	0.55	adult rat cardiac fibroblast	possibly via recruitment and Src phosphorylation	9486662	NIH-3T3 8668210		
middle	r67	Raf & !ERK => MEK1	1	1.3	0.55	adult rat cardiac fibroblast		12388314	NIH-3T3 8668210		21943356, 24489118
middle	r68	MEK1 & !PP1 => ERK	1	1.3	0.55	adult rat cardiac fibroblast		12388314	Cos1 cells 12167697		11259586, 15972258,
middle	r69	p38 => PP1	1	1.3	0.55	3T3 cells, adult and neonatal human dermal fibroblast	via activation	11259586	human endothelial cells 15972258	25659900	
middle	r70	MKK3 => p38	1	1.3	0.55	3T3 cells, adult and neonatal human dermal fibroblast	activation	11259586	human synoviocytes 15778394		
middle	r71	TGFB1R => TRAF	1	1.3	0.55	adult mouse cardiac fibroblast	activation	22749815	mouse embryonic fibroblasts 18922473		
middle	r72	Rac1 => MEKK1	1	1.3	0.55	NIH-3T3, HeLa	activation	7600582	ovarian cancer cells 9674706		
middle	r73	MEKK1 => MKK4	1	1.3	0.55	NIH-3T3, HeLa	activation	7600582	cos1, HeLa 12401521		
middle	r74	MKK4 & !NFKB => JNK	1	1.3	0.55	NIH-3T3, HeLa	activation	7600582	NIH-3T3 16076903		11713530, 11466617

Type	ID	Reaction				Cell	Description	Ref cell	PMID	PMID	PMID
middle	r75	PDGFR => abl	1	1.3	0.55	3T3	activation	16076903 mouse embryonic fibroblasts	10500097		
middle	r76	abl => Rac1	1	1.3	0.55	3T3	activation	16076903 mouse embryonic fibroblasts	15039778		
middle	r77	JNK => cmyc	1	1.3	0.55	3T3	activation	16076903 NIH-3T3	14523011		
middle	r78	cmyc => proliferation	1	1.3	0.55	3T3	activation	16076903 NIH-3T3	15195135		
middle	r79	TNFaR => TRAF	1	1.3	0.55	293 cells	activation	9774977 human cardiac fibroblast	17560598	10523862	
middle	r80	TRAF => ASK1	1	1.3	0.55	293 cells	activation - most likely binding allows the receptor to eventua	9774977 293, cos7, mouse embryonic fibroblas	10523862		
middle	r81	ASK1 => MKK3	1	1.3	0.55	COS7 cells	activation	8974401 human foreskin fibroblasts	10912795		
middle	r82	ASK1 => MKK4	1	1.3	0.55	COS7 cells	activation	8974401 human embryonic lung fibroblasts	19494316	9774977	
middle	r83	IL1RI => ASK1	1	1.3	0.55	fibroblast-like synoviocytes	assumed activation	15778394 human foreskin fibroblasts	10912795		
middle	r84	smad3 => PAI1	1	1.3	0.55	adult mouse cardiac fibroblast	transcription	17991884 Hep2g cells	9606191	11279127	
output	r85	NFKB => proMMP14	1	1.3	0.55	human dermal fibroblast	transcription	11112697 human breast cancer cell line	20855151		
middle	r86	Ras => p38	1	1.3	0.55	adult rat cardiac fibroblast	unknown	21367774 adult rat cardiac fibroblasts	14593117		
middle	r87	TGFB1R => PI3K	1	1.3	0.55	adult rat cardiac fibroblast	activation	21498085 NIH-3T3	16288034		
middle	r88	PDGFR => PI3K	1	1.3	0.55	3T3	activation	21943356 adult rat cardiac fibroblasts	11230972		
middle	r89	FAK => PI3K	1	1.3	0.55	human lung fibroblast	activation	15166238 human bone marrow mesenchymal ste	25900259		
middle	r90	TGFB1R => NOX	1	1.3	0.55	human cardiac fibroblast	activation	16179589 human dermal fibroblasts	26096997	25858818	
middle	r91	Akt => NFKB	1	1.3	0.55	human cardiac fibroblast	activation by removal of IKK	18064631 human dermal fibroblasts, rat synovioc	10485711		
output	r92	NFKB => fibronectin	1	1.3	0.55	human cardiac fibroblast	transcription	18064631 rat osteoblasts	17252537	23141425	
middle	r93	JNK => AP1	1	1.3	0.55	human periodontal ligament fibroblast	activation	21757573 neonatal cardiac fibroblasts	12695528		
middle	r94	IL1RI & TGFB => BAMBI	1	1.3	0.55	mice cardiac fibroblast	increased transcription (unsure of transcription factor)	24078695 adult rat cardiac fibroblasts	23734837		
middle	r95	Forskolin => AC	1	1.3	0.55	adult rat cardiac fibroblast	drug action	12711600 human lung fibroblast	15075208		
middle	r96	STAT => smad7	1	1.3	0.55	UA4 cell line	STAT necessary for smad expression	10067896 human lung fibroblast	11927620	22751114	
output	r97	SRF => proCI	1	1.3	0.55	10t1/2 cells, cardiac fibroblasts	MRTF directly activates the expression of COL1	20558820 NIH-3T3, mouse embryonic fibroblast	24732378		
middle	r98	Rho & !Rac1 => p38	1	1.3	0.55	neonatal rat cardiac fibroblast		21131638 murine mesangial cells	25007875		
middle	r99	MKK4 & !Rho => JNK	1	1.3	0.55	neonatal rat cardiac fibroblast		21131638 NIH-3T3	7600582		
output	r100	SRF => proCIII	1	1.3	0.55	mouse cardiac fibroblasts		20558820 NIH-3T3, mouse embryonic fibroblast	24732378		
output	r101	SRF & smad3 & CBP=> aSMA	0	1.3	0.55	human cardiac fibroblast		16179589 mouse embryonic fibroblasts	20558820	24732378	
middle	r102	calcineurin => NFAT	1	1.3	0.55	mouse cardiac fibroblasts	activation/nuclear translocation	22403241 neonatal mouse cardiac fibroblast	23178899		
middle	r103	AT1R => Ras	1	1.3	0.55	neonatal cardiac fibroblast		9486662 adult cardiac fibroblast	21367774		
output	r104	smad3 & CBP => aSMA	1	1.3	0.55	human cardiac fibroblast	txn activation	16179589 rat gingival fibroblasts	26738448		
output	r105	SRF=> aSMA	1	1.3	0.55	rat cardiac fibroblasts	transcription	17456553 mouse embryonic fibroblasts	15855636		
middle	r106	ETAR => DAG	1	1.3	0.55	rat embryonic fibroblasts	production	1809396 mouse embryonic fibroblasts	10676846		
middle	r107	AT1R => DAG	1	1.3	0.55	CHO cells	production	7653525 rat cardiac fibroblasts	17982962		
middle	r108	DAG => TRPC	1	1.3	0.55	human cardiac fibroblast	activation	17533154 adult rat cardiac fibroblasts	22992321	25521631	
middle	r109	TRPC & tension => Ca	1	1.3	0.55	human cardiac fibroblast	channel opening	23827314 adult rat cardiac fibroblasts	22992321		
middle	r110	Ca => calcineurin	1	1.3	0.55	adult rat cardiac fibroblast	activation	26191219 rat dermal fibroblasts	23022034		
middle	r111	TGFB1R => Rho	1	1.3	0.55	human gingivial fibroblasts		16953819 human colonic fibroblasts	24280883	29700112	
middle	r112	B3int => Src	1	1.3	0.55	human lung fibroblasts	dephosphorylation: Y530, autophosphorylation: Y419	18353785 CHO cells	14593208		
middle	r113	B1int => FAK	1	1.3	0.55	mouse embryonic fibroblasts, COS7	autophosphorylation: Y397	7529876 mouse embryonic fibroblasts	10413676	23589296	
middle	r114	FAK & Src => Grb2	1	1.3	0.55	mouse embryonic fibroblasts	activation via Src	7997267 mouse embryonic fibroblasts	9032297	8816475	
middle	r115	Grb2 => Ras	1	1.3	0.55	rat cardiac fibroblasts	activation via SOS	9486662 mouse embryonic fibroblasts, HEK293	8479541	7997267	
middle	r116	FAK & Src => RhoGEF	1	1.3	0.55	mouse embryonic fibroblasts	activation	18195107 mouse embryonic fibroblasts	18303050	19339545	
middle	r117	!Src => RhoGDI	1	1.3	0.55	mouse embryonic fibroblasts, HeLa	phorphorylation: decreases binding Rho binding affinity	16943322 293T	19321744		
middle	r118	FAK & Src => p130Cas	1	1.3	0.55	mouse embryonic fibroblasts	activation via Src	9032297 CHO cells	9425168	16581250	
middle	r119	PDGFR => Src	1	1.3	0.55	mouse embryonic fibroblasts	activation	8356071 mouse embryonic fibroblasts	10222144	9739761	
middle	r120	tension & Src => p130Cas	1	1.3	0.55	mouse embryonic fibroblasts	activation	8670206 mouse embryonic fibroblasts	22499769	17129785	
middle	r121	p130Cas & abl => Rac1	1	1.3	0.55	HEK293	activation	10385525 293T	18793427	17533370	
middle	r122	Factin => YAP	1	1.3	0.55	mouse embryonic fibroblasts	nuclear translocation	23644383 mouse embryonic fibroblasts	26757814	24648494	
middle	r123	PKA => RhoGDI	1	1.3	0.55	rat cardiac fibroblasts	phosphorylation	23012358 COS7 cells	18768928		
middle	r124	RhoGEF & !RhoGDI => Rho	1	1.3	0.55	mouse embryonic fibroblasts	activation	18303050 mouse embryonic fibroblasts	22649559	24467208	
output	r125	YAP => CTGF	1	1.3	0.55	rat embryonic fibroblasts	txn via TEAD	18579750 MCF10A	19324877	29563341	
middle	r126	syndecan4 => PKC	1	1.3	0.55	rat embryonic fibroblasts	activation	22504297 rat embryonic fibroblasts	12571249	16787950	
middle	r127	!PKC => RhoGDI	1	1.3	0.55	rat embryonic cardiomyocytes	phosphorylation	15316932 human umbilical vein endothelial cells	11309397		
middle	r128	!Gactin & NFAT => MRTF	0	1.3	0.55	mouse cardiac fibroblasts	translocation	23178899 mouse dermal fibroblasts	23022034		
middle	r129	!Gactin & Hic5 => MRTF	1	1.3	0.55	mouse embryonic fibroblasts	translocation	18025109 mouse embryonic fibroblasts	12475943	12475943	26759173
middle	r130	ROCK & Gactin => Factin	1	1.3	0.55	rat cardiac fibroblasts	polymerization	17456553 mouse embryonic fibroblasts	12732141	26721596	
middle	r131	!Factin => Gactin	1	1.3	0.55	mouse embryonic fibroblasts	polymerization	12475943 mouse embryonic fibroblasts	12732141		
middle	r132	MRTF => SRF	1	1.3	0.55	mouse embryonic fibroblasts		22461426 mouse embryonic fibroblasts	12732141	26721596	
fback	r133	!TNC & tension => syndecan4	1	1.3	0.55	mouse dermal fibroblasts	dephosphorylation	15483051 T98G	11731446	19339214	
middle	r134	Akt => mTORC1	1	1.3	0.55	HEK293	activation via TSC1/2, PRAS40 inhibition	12172553 mouse embryonic fibroblasts	16027121	19117990	
middle	r135	mTORC1 => p70S6K	1	1.3	0.55	mouse embryonic fibroblasts	activation	21602892 mouse embryonic fibroblasts	16027121	19117990	
middle	r136	!mTORC1 => EBP1	1	1.3	0.55	mouse embryonic fibroblasts	phosphorylation	23940704 HEK293	9465032	29518028	
middle	r137	!EBP1 & p70S6K => proliferation	1	1.3	0.55	rat cardiac fibroblasts	mRNA translation	16270752 human lung fibroblasts	21784851	15522879	
middle	r138	Akt => smad3	1	1.3	0.55	mouse embryonic fibroblasts	activation via GSK3B inhibition	24899689 mouse embryonic fibroblasts	19458083	17604717	
output	r139	NFKB => TNC	1	1.3	0.55	human cardiac fibroblasts	txn	23454256 chick embryonic fibroblasts	15363633	20107185	
output	r140	MRTF => TNC	1	1.3	0.55	human cardiac fibroblasts	txn	21705668 chick embryonic fibroblasts	15363633		
middle	r141	!p70S6K => mTORC2	1	1.3	0.55	mouse embryonic fibroblasts	phosphorylation via Rictor	19995915 HEK293	19720745		
middle	r142	mTORC2 & PI3K => Akt	1	1.3	0.55	mouse embryonic fibroblasts	activation	23311350 mouse embryonic fibroblasts	18566587	15718470	
middle	r143	mTORC2 & DAG => PKC	1	1.3	0.55	HEK293	activation	15268862 mouse embryonic fibroblasts	18566587	17604717	18566587
output	r144	YAP => PAI1	1	1.3	0.55	human lung fibroblasts	txn	25502501 mouse embryonic fibroblasts	27881410		
middle	r145	smad3 => thrombospondin4	1	1.3	0.55	human dermal fibroblasts	txn	30132849 mouse dermal fibroblasts	28481870		
fback	r146	!thrombospondin4 & tension => B3int	1	1.3	0.55	mouse cardiac fibroblasts	receptor binding	25897545 human ligament fibroblasts	19647831	20884877	19805288
output	r147	NFKB & AP1 & !smad3 => proMMP8	1	1.3	0.55	mouse mesenchymal stem cells	txn	30686120 human mesenchymal stem cells	24738865		
output	r148	NFKB & AP1 & !smad3 => proMMP3	1	1.3	0.55	mouse cardiac fibroblasts	txn	30686120 human cardiac fibroblasts	20619343	17706606	
output	r149	AP1 => osteopontin	1	1.3	0.55	rat cardiac fibroblasts	txn	14755545 rat lung fibroblasts	16211580		
fback	r150	osteopontin => B3int	1	1.3	0.55	rat cardiac fibroblasts	receptor binding	8941637 human lung fibroblast	16128620		
output	r151	CREB => proMMP12	1	1.3	0.55	human dermal fibroblasts	txn	23671273			
middle	r152	AP1 & !YAP => smad7	1	1.3	0.55	human dermal fibroblasts	txn: YAP/TAZ knock-down required for smad7 expression	29695252 mouse embryonic fibroblasts	11402315	10843994	
middle	r153	FAK & Src & MLC => paxillin	1	1.3	0.55	human foreskin fibroblasts	activation	20308429 mouse embryonic fibroblasts, PAEC	17164291		
middle	r154	vinculin & !paxillin => FA	1	1.3	0.55	human foreskin fibroblasts	stabilization: paxillin increases FA turnover for increased mig	18056416 mouse embryonic fibroblasts, PAEC	17164291		
middle	r155	B1int => talin	1	1.3	0.55	mouse embryonic fibroblasts	activation	18056416 mouse embryonic fibroblasts	27065098		
middle	r156	B3int => talin	1	1.3	0.55	mouse embryonic fibroblasts	activation	27065098 mouse fibroblast-like cells	14581461		
middle	r157	talin & contractility => vinculin	1	1.3	0.55	mouse embryonic fibroblasts	activation	18056416 mouse embryonic fibroblasts	27065098		
middle	r158	Factin & MLC => contractility	1	1.3	0.55	mouse embryonic fibroblasts	binding via vinculin tail region	18056416 mouse embryonic fibroblasts	23716647		
fback	r159	contractility & FA => tension	1	1.3	0.55	human foreskin fibroblasts	force generation via molecular clutch theory	28592635 human foreskin fibroblasts	23859772	26121555	
middle	r160	ROCK => MLC	1	1.3	0.55	mouse embryonic fibroblasts	activation via MLCK activation, MBS inhibition	10953004 rat embryonic fibroblasts	16043513		

middle	r161	Cilia => PKD1	1	1.3	0.55	mouse embryonic kidney cells	direct co-localization in WT at basal body and ciliary tubulin	12514735	mouse kidney epithelium	12239239			
middle	r162	Cilia => PKD2	1	1.3	0.55	mouse kidney cells	direct co-localization in WT at basal body and ciliary tubulin	12062067	mouse embryonic kidney cells	12514735			
middle	r163	Cilia & tension => PKD1	1	1.3	0.55	VSMCs	PKD1 needed for response to inc pressure	19879844	chondrocytes (cyclic)	22223751			
middle	r164	PKD1 => PKD2	1	1.3	0.55	mouse embryonic kidney cells	direct co-localization in WT at basal body and ciliary tubulin	12514735	COS cells, kidney epithelium, aortic epit	19879844			
middle	r165	PKD2 => TRPV4	1	1.3	0.55	mouse endothelial cells	tension = shear stress	19265036	kidney epithelial cells	12514735	18695040	keratinocytes	29610016
middle	r166	PKD2 & tension => NOX	1	1.3	0.55	mouse endothelial cells	tension = shear stress	19265036	primary osteocytes	24268313			
middle	r167	TRPV4 & tension => Ca	1	1.3	0.55	pulmonary adventitial fibroblasts		31693393	pulmonary fibroblasts	29126921			
middle	r168	PKD1 & B1int => FAK	1	1.3	0.55	medullary collecting duct cells	co-ip and activation when plated on fibronectin	16790429	MDCK cells	25947155			
middle	r169	PKD2 => IP3R	1	1.3	0.55	Xenopus cells		16223735	human kidney epithelium	22456092			
middle	r170	PKD2 & IP3R => Ca	1	1.3	0.55	Xenopus cells		16223735	human kidney epithelium	22456092			
middle	r171	Cilia => DZIP1	1	1.3	0.55	valve interstitial cell	co-immunoprecipitation	31118289	mouse embryonic fibroblasts	23955340			
middle	r172	DZIP1 => CBY1	1	1.3	0.55	valve interstitial cell	co-immunoprecipitation	Guo et al. 2020	confirmed with yeast 2-hybrid screen				
middle	r173	!CBY1 => Bcatenin	1	1.3	0.55	valve interstitial cell	cby1 knockdown leads to increased nuclear B-catenin	Guo et al. 2020	mouse respiratory epithelium	19364920	12712206	18573912	
input	i12	=> DHH	0.1	0.55		increased during cardiac development		32151560					
middle	r174	Cilia & DHH & !Ptch1 => SMO	1	1.3	0.55	valve interstitial cell		28556366	valve interstitial cell	32151560	17641202	22474285	
middle	r175	SMO => TIAM1	1	1.3	0.55	valve interstitial cell		32151560	mouse embryonic fibroblasts, pyramida	20654717			
middle	r176	TIAM1 => Rac1	1	1.3	0.55	valve interstitial cell		32151560	human dermal fibroblasts	20802514			
middle	r177	Cilia & PDGF => PDGFR	0.25	1.3	0.55	MEFs		20110426	NIH3T3 cells	16243034			
input	i13	=> WNT	0.1	0.55		increased during cardiac development and matrix production		22819513					
middle	r178	Cilia & TGFB => TGFB1R	0.25	1.3	0.55	mouse embryonic fibroblasts	dec cilia => dec receptor function	23746451	mesenchymal stem cells	27748449			
fback	r179	periostin => B1int	1	1.3	0.55	valve interstitial cell		30742951	valve interstitial cell	24469446			
middle	r180	Akt => Pak1	1	1.3	0.55	valve interstitial cell		30742951	valve interstitial cell	24469446			
fback	r181	periostin => B3int	1	1.3	0.55	valve interstitial cell		24469446	valve interstitial cell	30742951			
middle	r182	Flna & tension => B1int	1	1.3	0.55	HEK293	FLNA binds to cytoplasmic tail of B1int	18177638	T cells	9722563			
middle	r183	Rac1 => Pak1	1	1.3	0.55	Human 293T cells	rac1 needed for activation of Pak1 at membrane	11804587	Fibroblasts	11134074			
middle	r184	Pak1 => ERK	1	1.3	0.55	valve interstitial cell		24469446	mouse medullary collecting cells	23781022			
middle	r185	Pak1 => Flna	1	1.3	0.55	3T3 fibroblasts	co-immunoprecipitation	32389644	MCF-7 cells	12198493			
middle	r186	FAK => Hic5	1	1.3	0.55	293T cells		9858471	rat fibroblast (WFB)	9422762			
middle	r187	SMO => Gli2	1	1.3	0.55	Valve interstitial cell		32151560	vascular adventitial fibroblasts	29088375			
middle	r188	Gli2 => Runx2	1	1.3	0.55	osteoblast		17442891	mouse fetal cardiac cells	18813803			
middle	r189	Runx2 => ADAMTS5	1	1.3	0.55	chondrocytes		21094261	synovial fibroblasts	27449198			
middle	r190	Runx2 => ADAMTS4	1	1.3	0.55	Chondrocytes		21094261	synovial fibroblasts	27449198			
middle	r191	Runx2 => ADAMTS9	1	1.3	0.55	chondrocytes		21094261	synovial fibroblasts	27449198			
middle	r192	Runx2 => proMMP13	1	1.3	0.55	chondrocytes		21094261	chondrocytes	16868966			
middle	r193	!tension => Cilia	1	1.3	0.55	tenocytes	cyclic stress lead => cilia length	20957738	chondrocytes (cyclic)	24457103	human endothelial cells	15024030	
middle	r194	Cilia & Gactin => Factin	0.25	1.3	0.55	chondrocytes	cilia loss is associated with decreased F-actin organization	26493329	chondrocytes	17359961			
middle	r195	WNT & Cilia => Fz	1	1.3	0.55	mouse cardiac fibroblasts		30040870	conserved across species and cell types	19147006			
middle	r196	Fz => Dvl	1	1.3	0.55	mouse cardiac fibroblasts		30040870	conserved across species and cell types	19147006			
middle	r197	!Dvl => GSK3B	1	1.3	0.55	mouse cardiac fibroblasts		30040870	conserved across species and cell types	19147006			
middle	r198	!GSK3B => Bcatenin	1	1.3	0.55	mouse cardiac fibroblasts		30040870	conserved across species and cell types	19147006			
middle	r199	!Bcatenin => Groucho	1	1.3	0.55	mouse cardiac fibroblasts		30040870	conserved across species and cell types	19147006			
middle	r200	!Groucho => TCF	1	1.3	0.55	mouse cardiac fibroblasts		30040870	conserved across species and cell types	19147006			
middle	r201	!Cilia => Bcatenin	1	1.3	0.55	MEFs		18084282	MEFs	21602792			
middle	r202	Rac1 & smad3 => NOX	1	1.3	0.55	NIH-3T3	Rac activates Nox	8809022	VSMC	16514078			
middle	r203	NOX => MLC	1	1.3	0.55	mouse myofibroblasts		24403605	lung VSMC	18621909			
middle	r204	Bcatenin & MRTF => SRF	1	1.3	0.55	LLC-PK1 cells	potentially through a de-repressor action	21965288	MCF-7 cells	29632640			
middle	r205	TCF => fibronectin	1	1.3	0.55	mouse lung fibroblasts		15617677	embryonic stem cells	18983966			
middle	r206	TCF => versican	1	1.3	0.55	VSMCs		15668231	human melanoma cells	19269971			
middle	r207	aSMA & MLC => contractility	1	1.3	0.55	mouse myofibroblasts		19800625	rat lung fibroblasts	18086923			
fback	r208	tension & latentTGFB => TGFB	0.25	1.3	0.55	rat lung fibroblasts	contraction & stretch can release active TGFb from LBP	18086923	HCC cells	28025149			

Supplemental Figure Legends:

Figure S1: Regional fibrosis in MVP patients. (A) Patient age and leaflet involvement are listed. **(B)** Masson's histochemical stain at low magnification showing entire biopsy region and prominent fibrosis (blue) in peri-papillary region compared to within-person tissues from either apex or septum. **(C)** Same patient biopsies immunostained for collagen I (black). Scale bars = 1mm.

Figure S2: Evidence of sarcomeric loss in myocytes. Biopsy from MVr patient shows well elaborated myocytes (purple) with definable sarcomeric organization and no detectable fibrosis within the apex region. Within the same patient, prominent fibrosis and sarcomeric disorganization/loss (arrows) are prominent within fibrotic (collagen-yellow) zones in peri-papillary regions. Scale bars are 50μm.

Figure S3: Regional fibrosis correlates with increased macrophages in MVP. Septal (top) and peri-papillary biopsies were obtained from the same patient during MVr and IHC was performed for collagen (yellow), CD163 (purple) and nuclei (Hoecsht-blue). Uniquely within the peri-papillary region, prominent fibrosis and CD163^{+} macrophages are observed.

Figure S4: Full network of all input nodes used in computational modeling. Interconnections between all nodes from >300 publications of cardiac fibroblast molecular and mechanobiology were interpolated.

Figure S5: Heat map of all significant differentially expressed genes. 232 statistically significant differentially expressed genes between stretched and static human cardiac fibroblasts are represented.

Supplemental Video Legends:

Video S1: 2D TEE echocardiography showing prominent posterior leaflet prolapse

Video S2: 3D TEE echocardiography showing prominent posterior leaflet prolapse

Video S3 and S4: Cardiac MRI with late gadolinium enhancement showing evidence of peri-papillary and inferobasal myocardial fibrosis

Video S5: Mitral valve repair showing prominent anterior leaflet prolapse and gross inspection of intramyocardial papillary fibrosis (white dense material) and absence of fibrosis in the apex tissue. Yellow color = fat

A

Patient	Age	Leaflet Involvement
MI-LVF-001	62	P2
MI-LVF-002	53	P1, P2, P3
MI-LVF-003	55	P2
MI-LVF-004	69	P2
MI-LVF-005	61	A2, P2
MI-LVF-006	58	A3, P3

B

C
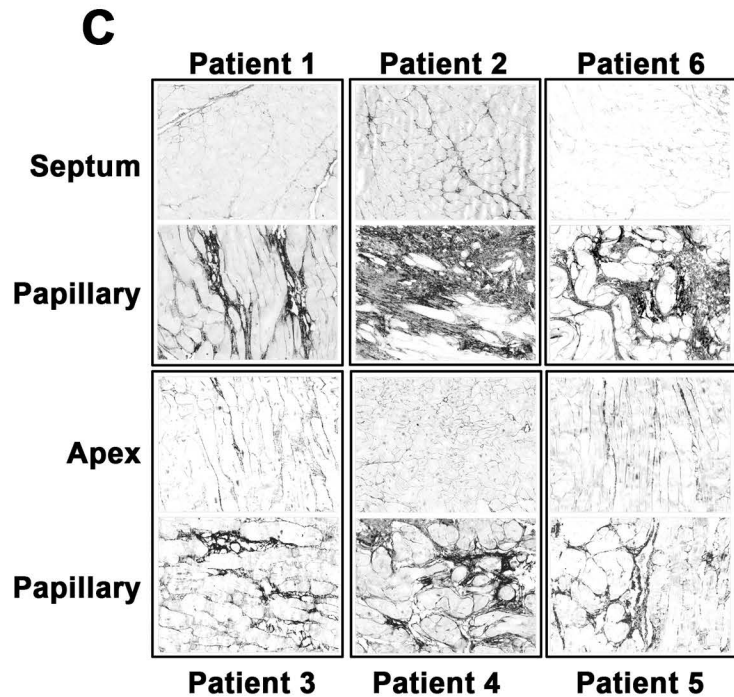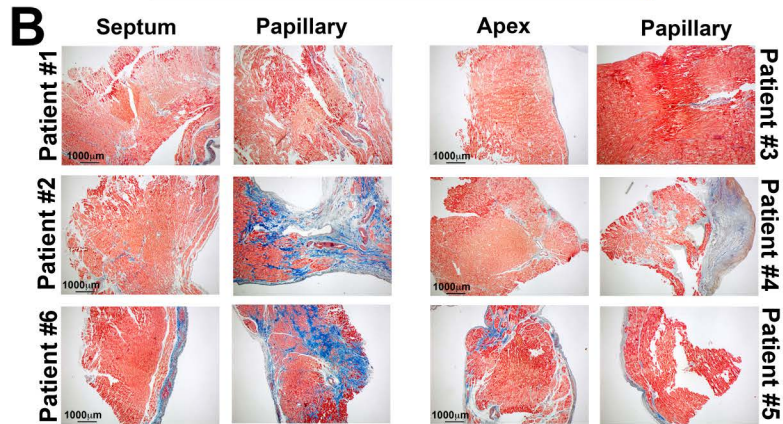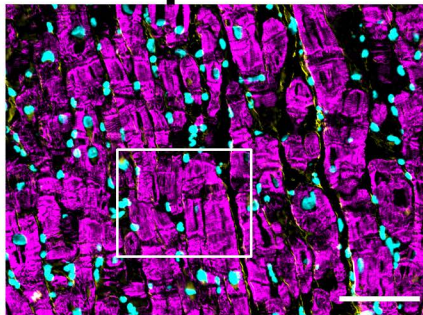
Figure S1

Apex | **Papillary**
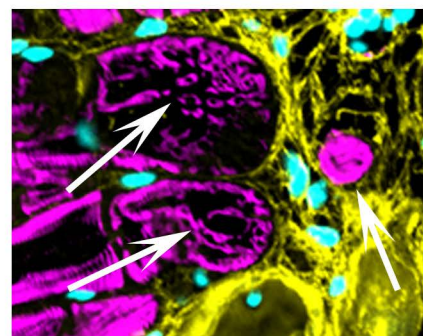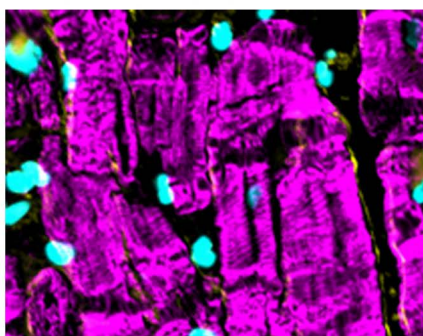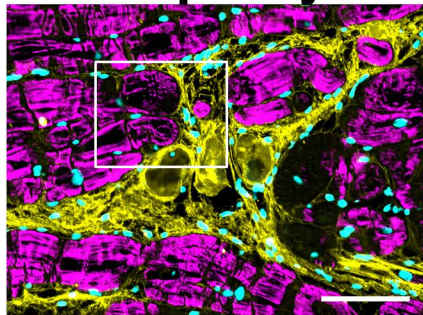
Collagen/**Myocytes**/**Nuclei**

Figure S2

Septum
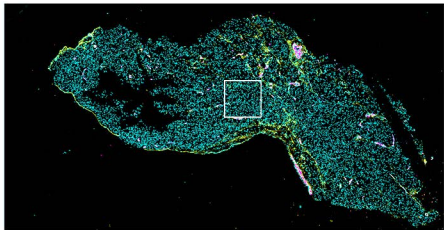
Papillary
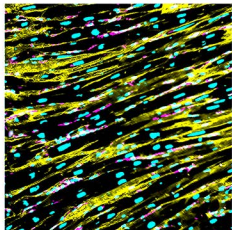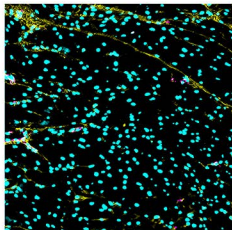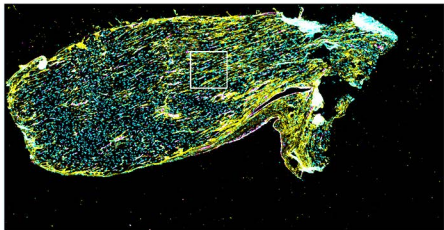
Collagen/CD163/Hoechst

Figure S3

Figure S4